JOURNAL OF GEOPHYSICAL RESEARCH, VOL. 117, D07113, doi:10.1029/2011JD017025, 2012

Mesospheric concentric gravity waves generated by multiple convective storms over the North American Great Plain

Sharon Vadas,[1] Jia Yue,[2] and Takuji Nakamura[3]

Received 17 October 2011; revised 24 January 2012; accepted 22 February 2012; published 14 April 2012.

[1] We report on six continuous hours of OH airglow imager observations (at z ~ 87 km) of convectively generated gravity waves (GWs) near Fort Collins, Colorado, on the evening of 08 September 2005. These GWs appeared as nearly concentric rings, and had epicenters near the locations of deep convection in three thunderstorms in Colorado, Nebraska and South Dakota. Using GOES satellite and weather radar observations, we show that the GWs closely follow the thunderstorms. Using the background wind from a nearby radar, the intrinsic wave parameters and vertical wavelengths are calculated. The temperature perturbations are estimated to be $T'/\overline{T} \sim$ 1–3% for GWs with horizontal wavelengths $\lambda_h \sim$ 20–40 km and horizontal phase speeds ~40–60 m/s. The horizontal wavelengths of GWs from a convective cluster decreased in time from 30 to 15 km. We employ convective plume and ray-trace models to simulate the GW-induced OH intensity perturbations from convective plumes, clusters and complexes. We find that the results using the background model wind (radiosonde/TIME-GCM) agree well with the late-time observations, when the images are dominated by southwestward, short-wavelength, high-frequency GWs. These late-time GWs propagate against the background wind, and have $\lambda_h \sim$ 30–40 km and periods of $\tau \sim$ 20–30 min. The OH intensity perturbations are enhanced because the vertical wavelengths λ_z increased, $T'/\overline{T}$ increased, and the vertical velocity perturbations w' decreased (because the GWs were near their reflection levels). We also find that these short-wavelength GWs were created ~5 h earlier by an extremely energetic, deep convective plume in South Dakota, thereby showing that small-scale, convective GWs directly link the troposphere and mesopause region.

Citation: Vadas, S., J. Yue, and T. Nakamura (2012), Mesospheric concentric gravity waves generated by multiple convective storms over the North American Great Plain, *J. Geophys. Res.*, *117*, D07113, doi:10.1029/2011JD017025.

1. Introduction

[2] Atmospheric gravity waves (GWs) and their dissipation through wave breaking/saturation are recognized to play a major role in the general circulation, temperature, and constituent structure of the mesosphere and lower thermosphere (MLT) [*Lindzen*, 1981; *Holton*, 1982; *Garcia and Solomon*, 1985]. To properly account for the momentum and energy budget of the middle atmosphere, and to investigate the lower-upper atmosphere coupling, it is important to characterize the sources, propagation and damping of GWs within the atmosphere.

[3] Deep convection (i.e., strong thunderstorms) can frequently excite gravity waves in the lower atmosphere during the spring, summer and fall months [e.g., *Holton and Alexander*, 1999]. During a strong thunderstorm, an energetic, warm and moist plume can rise rapidly in a convectively unstable environment to the tropopause. If energetic enough, the plume can overshoot the tropopause by up to 1–3 km into the stably stratified stratosphere, where it thereafter collapses and spreads out horizontally as an anvil at the tropopause [*Lane et al.*, 2001; *Wallace and Hobbs*, 2006]. This overshooting displaces the air in the stable environment from equilibrium, exciting GWs. At the same time, diabatic forcing (latent heating and cooling) in the lower stratosphere also excites high-frequency GWs [*Alexander et al.*, 1995; *Pandya and Alexander*, 1999; *Beres*, 2004]. These processes excite a broad spectrum of GWs that have a large range of temporal and spatial scales [e.g., *Pierce and Coroniti*, 1966; *Holton and Alexander*, 1999; *Lane et al.*, 2001; *Song et al.*, 2003; *Choi et al.*, 2007; *Vadas et al.*, 2009a, 2009b].

[4] While radiating away from the plume, GWs may imprint their concentric-ring shape on the cumulus clouds. For example, a 30-mile-wide storm cloud with small-scale concentric rings over the coast of Nigeria was seen from the space shuttle Columbia during NASA's STS-55 mission

---

[1] NorthWest Research Associates, Inc., Boulder, Colorado, USA.
[2] High Altitude Observatory, National Center for Atmospheric Research, Boulder, Colorado, USA.
[3] National Institute of Polar Research, Tokyo, Japan.

0148-0227/12/2011JD017025

on 2 May 1993 [*Pitts et al.*, 1995]. As concentric GWs propagate upward from the tropopause/lower stratosphere, their phases show a conical shape in the vertical cross-section centered near their sources [*Alexander et al.*, 1995, 2004; *Piani et al.*, 2000; *Horinouchi et al.*, 2002; *Lane et al.*, 2003; *Vadas and Fritts*, 2004]. On a horizontal plane above a convective source, the perturbations in temperature, air density, and velocity appear as outward expanding concentric rings if the intervening winds are "small" [*Vadas and Fritts*, 2009]. The radiation from CO_2 4.3-μm vibrational transitions (peaking at 40 km) sometimes show circular or elliptical patterns above thunderstorms, as viewed from space because the temperature and air density are perturbed by GWs [*Dewan et al.*, 1998; *Grimsdell et al.*, 2010; *Hoffmann and Alexander*, 2010]. The smaller-scale GWs in the excited spectrum often break or reach critical levels in the stratosphere or lower mesosphere [*Lane et al.*, 2003; *Lane and Sharman*, 2006]. Some convective GWs with somewhat larger scales, faster phase speeds and smaller amplitudes may penetrate to the mesopause region (80–105 km). There, they may reach critical levels, become evanescent and reflect downward, or propagate into the thermosphere. These GWs may also induce significant perturbations in the OH airglow emission, thus enabling their observation by ground-based airglow imagers [*Hecht et al.*, 1993; *Taylor et al.*, 1995, 2009; *Swenson et al.*, 1995; *Smith et al.*, 2000]. Significant modeling has been performed to understand how GWs perturb the OH layer [*Krassovsky*, 1972; *Hines and Tarasick*, 1987; *Walterscheid et al.*, 1987; *Hickey*, 1988a, 1988b; *Schubert and Walterscheid*, 1988; *Swenson and Gardner*, 1998; *Liu and Swenson*, 2003; *Hickey and Brown*, 2002; *Hickey and Yu*, 2005]. If the intervening winds are "weak," these GWs can appear as concentric circular patterns even at this altitude [*Taylor and Hapgood*, 1988; *Sentman et al.*, 2003; *Suzuki et al.*, 2007; *Yue et al.*, 2009] (final reference is cited as Y09 hereafter).

[5] During the deployment of an all-sky OH airglow imager at the Yucca Ridge Field Station (YRFS), Colorado (40.7N, 104.9W) between 2003 and 2008, 9 nights of concentric GWs were observed at z $\sim$ 87 km in the OH layer (see detailed introduction in Y09). Nearly all of these GW events occurred near the equinoxes when the intervening background wind between the tropopause and mesopause was $\sim$20 m/s or smaller. Beneath the epicenters of these concentric rings, strong convective plumes were found $\sim$1 h prior to the observations of these GWs. Among the nine events, a simple case on 11 May 2004 was selected in order to conduct a comparative study between the observations and modeling. The concentric GWs on this particular night were excited when two single, nearly co-located ($\sim$80 km apart) deep convective plumes overshot the tropopause nearly simultaneously. These results were reported by Y09 and *Vadas et al.* [2009a] (hereafter V09). Those works investigated the horizontal wavelengths and apparent periods of the GWs as a function of radius (defined as the distance between the epicenter of the concentric ring and the wave phase front) and propagation time (the time between the plume overshoot and the wavefront observation). Overall, the observations and numerical modeling of the concentric GWs excited by the convective plumes agreed reasonably well.

[6] Among the 9 nights of concentric GW observations, the concentric GWs on the night of 8 September 2005 were perhaps the most complex, interesting and unique. On this night, the ring patterns were observed continuously for $\sim$6 h, and there were distinct ring patterns from three different storm systems separated by hundreds of kilometers over the Great Plain of North America. Because of the constructive and destructive interference in the airglow images from these concentric GWs, as well as the continued creation of new concentric GWs from new plumes for many hours, it is more difficult to analyze these GWs than those in Y09. Yet long-duration, simultaneous thunderstorms often take place on the Great Plain and in other locations. Although the intervening wind is not usually weak enough to preserve the concentric ring-like appearance of the GWs near the mesopause, a detailed investigation of the textbook-like wave patterns on 8 September 2005 can lead to a much better understanding of the wavelengths, periods and amplitudes of the GWs excited by deep convection. This is important for modeling the effects of convective GWs on the MLT and thermosphere. Additionally, whereas Y09 and V09 studied the GWs from single plumes, the thunderstorms here involve many strong clusters of plumes. Because the cluster model encompasses several simplifying assumptions [*Vadas et al.*, 2009b], and because clusters are commonplace in strong convective thunderstorms, this study is also important for testing and tuning the cluster model.

[7] In this paper, we investigate the concentric GWs observed on 8 September 2005. We also identify their convective sources in the troposphere. Using background wind measurements at z $\sim$ 90 km by the medium frequency (MF) radar, we also estimate the GW intrinsic wave parameters, vertical wavelengths and propagation times. We model the GWs excited by the plumes, clusters and complexes identified on the Geostationary Operational Environment Satellite (GOES) infrared (IR) satellite images, and ray-trace these GWs into the mesosphere using a model wind and a zero wind. The zero wind study is useful in order to separate mean wind and spectral amplitude effects. We then reconstruct the GW fields form the momentum fluxes, and calculate the resulting temperature and OH intensity perturbations using an analytic function representing the cancellation factor. We then compare the model results with the observations. We follow with a discussion and our conclusions.

2. Airglow Imager Observations

[8] The all-sky airglow imager at YRFS, Colorado, monitored nighttime OH airglow emissions around 87 km between 2003 and 2008. The imager is sensitive to the OH Meinel bands between 795 nm and 1 μm at the OH layer [*Nakamura et al.*, 2005; Y09]. One image is acquired every 2 min with 100 s exposure time. A brief introduction of the concentric GWs from all 9 nights, their estimated convection sources and background winds can be found in Y09. Here, we present a detailed discussion of the measured and calculated GW parameters and background wind effect on 8 September 2005.

[9] On 8 September 2005, the imager was turned on at 03 Universal Time (UT) or 21 Local time. Concentric elliptical patterns are clearly seen from the first raw image. Figure 1a shows a sample raw image at 0350 UT. Concentric rings are evident at the lower right-hand portion of the image. To remove the background light and stars, and to enhance

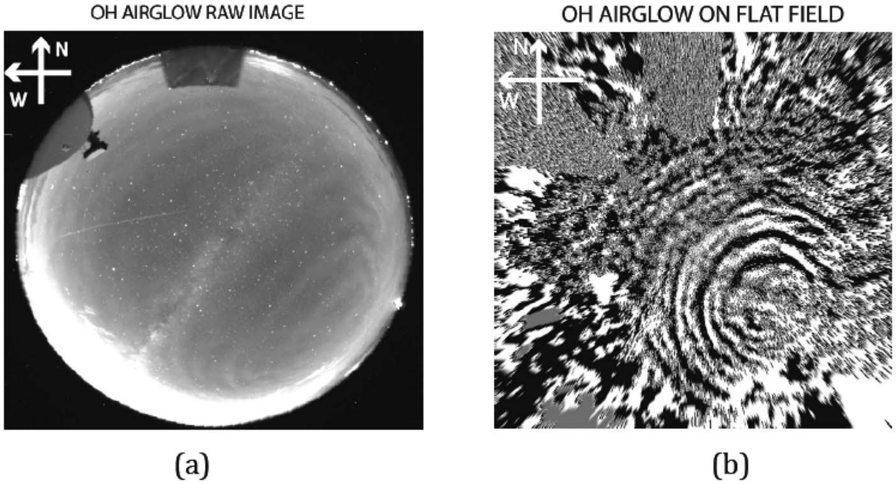

Figure 1. (a) OH raw image at 0350 UT, 8 September 2005. Top and left correspond to north and west, respectively. Elliptical rings radiate from the lower right corner. The bright band across the field of view is the Milky Way. The two shadows on the top are irrelevant objects installed near the imager on the ground. (b) Unwrapped difference image on a 800 km × 800 km area.

the GW structure, consecutive raw images are subtracted to create difference images. Then the difference images are unwrapped onto geographical coordinates. This algorithm was introduced by *Garcia et al.* [1997], and was applied in Y09. The unwrapped difference image on a flat geographic field for Figure 1a is shown in Figure 1b. We see that the elliptical rings are transformed into nearly circular rings. Another group of rings moving southwest(SW)ward from the upper right-hand corner is also visible in Figure 1b. Although a very large area of 800 km × 800 km is plotted in Figure 1b to display as many wave structures as possible, GWs at the edges are distorted, so their parameters cannot be measured accurately there.

[10] Selected flat-field OH images on 8 September 2005 (approximately 30 min apart) are displayed in Figure 2. An animation playing the sequence of all difference OH images during this night is provided as auxiliary material.[1] From 0300 to 0845 UT, the appearance of concentric GWs changed dramatically. At ~0300 UT, one group of concentric rings was centered on northeastern Colorado at (39N–40N, 101–103W). The southern portion of the rings were blocked by clouds (gray and white patches). Clouds in the raw images are noticeably brighter than the ambient airglow emissions and stars, and move through the imager field of view quickly. Additionally, clouds usually block stars and saturate the airglow images. By fitting (round) circles of different radii to each ring, we estimate each ring's epicenter, and show them as red dots in Figure 2. If the intervening wind between the tropopause and mesopause is negligible, these epicenters will coincide with the locations of the wave sources in the lower atmosphere. The only known common tropospheric source which can create symmetric, concentric rings of high-frequency GWs are deep convective plumes [e.g., *Piani et al.*, 2000; *Lane et al.*, 2001; *Vadas and Fritts*, 2009]. Point sources, such as earthquakes and nuclear explosions, also excite concentric GWs, although they are unusual. Horizontal body forces (created from the momentum deposited in the fluid when a GW breaks) also create concentric rings; however they are asymmetric, not symmetric (e.g., the amplitudes of the GWs parallel (perpendicular) to the force direction are maximum (zero)) [*Vadas et al.*, 2003]. For the 11 May 2004 event, Y09 traced the concentric GWs back to their sources, which were two adjacent single plumes. On that night and on 8 September 2005, the Thermosphere-Ionosphere-Mesosphere-Electrodynamics General Circulation Model (TIME-GCM) model climatological wind and radiosonde wind were smaller than 20 m/s at all altitudes [see Y09, Figures 7–9].

[11] The red dots in Figure 2a show that there may be multiple wave centers in the area of (39–40N, 101W–103W) if the intervening wind is negligible; this could be indicative of different convective plumes within a cluster or complex. Otherwise, temporally or spatially varying background winds can also lead to such an observation, since the wind Doppler shifts the GWs in each ring and each epicenter differently because the GWs in each ring have different frequencies and phase velocities (V09). We see this as follows. For zero background wind, the angle that a high-frequency, small-scale GW's phase front makes with the vertical is α, and is related to the GW's intrinsic frequency, ω_I, via [*Hines*, 1967],

$$\cos\alpha \sim \frac{\omega_I}{N} \tag{1}$$

where N is the Brunt-Vaisala frequency. If the background wind is constant in time, the apparent or observed GW frequency is constant in time [*Lighthill*, 1978]. For a vertical propagation distance from convective overshoot to the OH layer of Δz, and if the constant background wind is constant with altitude (or negligible), the radius of a GW in the horizontal plane of the OH layer is

$$R = \Delta z \tan\alpha = \Delta z\sqrt{(N/\omega_I)^2 - 1}. \tag{2}$$

---

[1] Auxiliary materials are available in the HTML. doi:10.1029/2011JD017025.

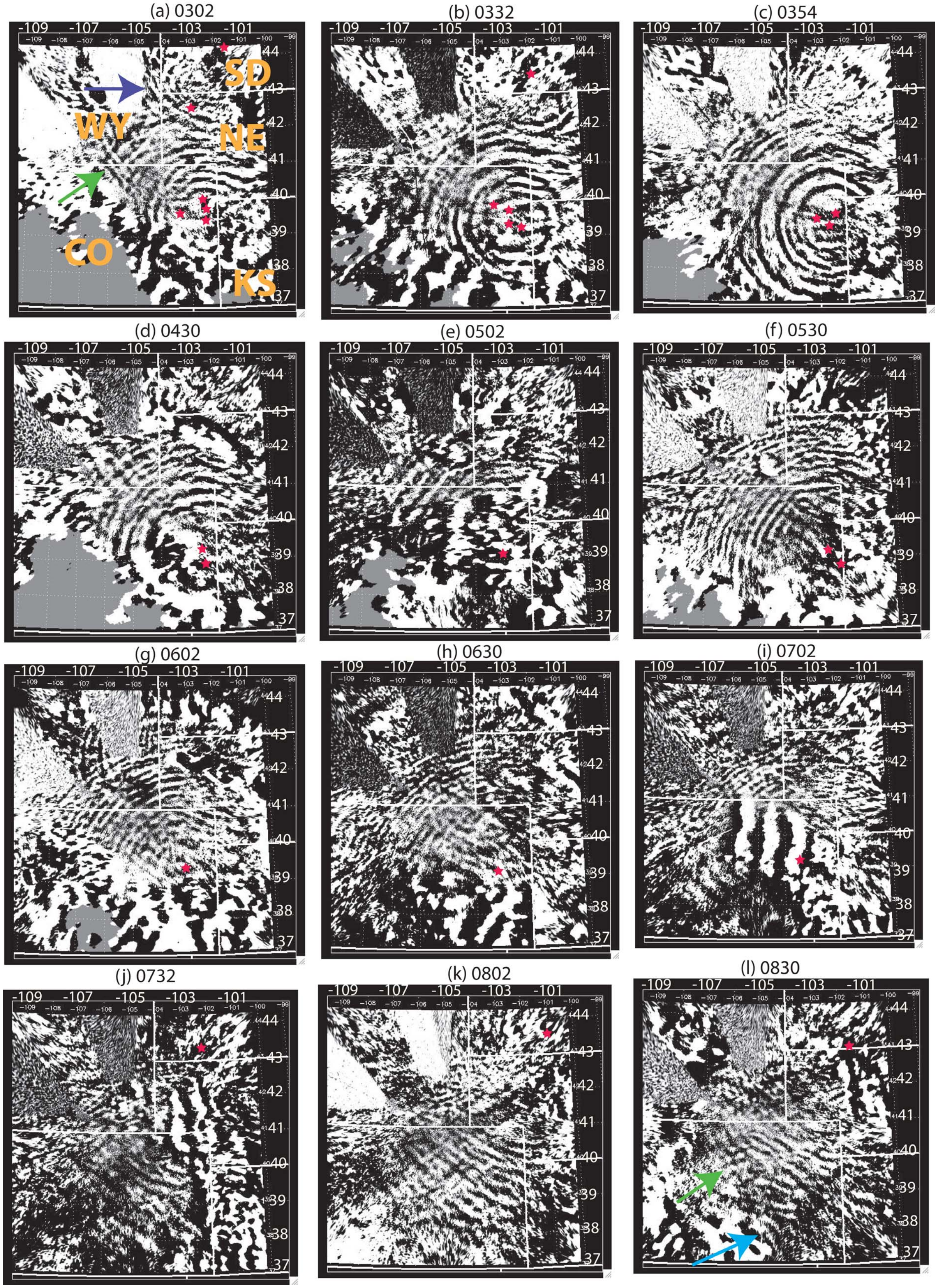

Figure 2. The 800 km × 800 km difference OH images from 0300 to 0830 UT on 08 September 2005. The while lines indicate the state borders between Colorado (CO), Nebraska (NE), Kansas (KS) and Wyoming (WY). The estimated centers of the rings are marked by red dots. Arrows indicate waves of interest (see text).

Therefore, the radius of a concentric GW ring only depends on its intrinsic period if the wind is constant or negligible. If the wind is negligible, then the red dots indicate multiple wave sources.

[12] From Figure 2a, we measure the horizontal wavelengths of the GWs at radii of R = 80–200 km (from 39 to 40N, 101W-103W) to be $\lambda_h \sim (26\text{–}30) \pm 4$ km. The measurement uncertainty of the wavelength depends on the quality of the images [Y09]. We also measure the apparent period τ to be 8 ± 1 min, and the apparent phase speed to be $c_h \sim 60 \pm 20$ m/s. A second group of concentric GWs with phase lines oriented northwest-southeastward (denoted by the green arrow in Figure 2a) are located in the region of (40–42N, 105–107W). Their horizontal wavelength, apparent period and apparent phase velocity are measured to be $\lambda_h \sim 20 \pm 4$ km, $\tau \sim 10 \pm 1$ min and $c_h \sim 34 \pm 10$ m/s, respectively. The fitted epicenter of these waves is located at (42.5N, 103W), in northwestern Nebraska. The radii of these waves is therefore $230\text{–}300 \pm 10$ km. A third group of concentric gravity waves are located at (42–43N, 101–105W), denoted by the blue arrow in Figure 2a. Their horizontal wavelengths, apparent periods and phase velocities are $\lambda_h \sim (26\text{–}30) \pm 4$ km, $\tau \sim 10 \pm 1$ min and $c_h \sim 45 \pm 15$ m/s, respectively. The fitted epicenter is located at (44N, 102W) in southwestern South Dakota, so these waves are approximately $R \sim 200 \pm 10$ km from their sources horizontally.

[13] The anelastic dispersion relation for a GW is [*Fritts and Alexander*, 2003]:

$$m^2 = \frac{N^2}{(c_h - U_h)^2} - k_h^2 - \frac{1}{4\mathrm{H}^2}, \tag{3}$$

where U_h, $k_h = 2\pi/\lambda_h$, and H are the background wind velocity in the wave propagation direction, horizontal wave number, and density scale height, respectively. H is estimated to be 6 km. With no concurrent temperature measurement, we assume a background buoyancy frequency of $N = 2\pi/(5\text{ min})$. On 11 May 2004, there were no background wind measurements at the mesopause (Y09). However, on 8 September 2005, a nearby 2 MHz MF radar was in operation at Platteville, Colorado (40.2N, 104.7W) to monitor the mesopause wind field [*Manson et al.*, 2003]. Figure 3 shows a hodograph of the background wind at 88 km between 0 and 9 UT. Radar wind data is not available below 88 km during the nighttime. At 3 UT, the background wind is southeastward with a magnitude of 38 ± 22 m/s. For the second and third groups of GWs propagating SWward in Figure 2a, the background wind is almost perpendicular to the GW propagation directions; therefore, for those GWs, $U_h \sim 0$. We use the dispersion relation in equation (3), and define the vertical wavelength to be $\lambda_z = 2\pi/m$. For the second and third group of GWs, $|\lambda_z| \sim 11 \pm 3$ km and 15 ± 5 km, respectively. We note that the uncertainty of the MF wind is not considered here for simplicity. As the first group of concentric GWs propagated from (39–40N, 101W-103W) in all directions, the vertical wavelengths of the individual GWs depend on the direction of propagation and on the intrinsic horizontal phase velocity $c_h - U_h$. For the westward propagating GWs, the average $|\lambda_z|$ is 37–53 km with a large uncertainty of ~15 km. The northward propagating GWs have imaginary m and become evanescent when considering the background radar wind.

[14] The vertical group velocity of a GW is $c_{gz} \sim \delta\omega_I/\delta m$, where the intrinsic frequency is $\omega_I = k_h(c_h - U_h)$. Using equation (3), which can be rewritten as $\omega_I^2 = (k_h N)^2/(m^2 + k_h^2 + 1/4\mathrm{H}^2)$, the vertical group velocity of a GW is

$$c_{gz} \sim -m\omega_I/(m^2 + k_h^2 + 1/4\mathrm{H}^2) \sim -m\omega_I^3/(k_h N)^2 \sim \lambda_h^2 \tau_B^2/(|\lambda_z| \tau_I^3), \tag{4}$$

where $\tau_B = 2\pi/N$ is the buoyancy period. Therefore, the smaller horizontal wavelength of $\lambda_h \sim 20$ km and a larger radii of $R \sim 230\text{–}300$ km (i.e., larger $\tau_I = 2\pi/\omega_I$) for the GWs in the second group implies a slower vertical group velocity and longer propagation time than the GWs in the first group. Since the OH layer height is ~87 km and the tropopause height is 16 km, using $\Delta z \sim 87\text{–}16 \sim 71$ km, we estimate vertical propagation times from the tropopause to the OH layer of $\Delta t = \Delta z/c_{gz} \sim (20\text{–}38) \pm 15$ min, 96 ± 29 min, and 75 ± 28 min for the GWs in groups 1, 2, and 3, respectively. This implies source times of ~0205–0255 UT, 0100–0155 UT and 0120–0215 UT, respectively. Note that the GWs in groups 2 and 3 were likely excited earlier than those in group 1.

[15] Because the thickness of the OH layer is 8–9 km, the airglow intensity perturbation in the OH layer can be quite small for GWs with short vertical wavelengths because of destructive interference of the positive and negative wave fluctuations [*Hines and Tarasick*, 1987; *Taylor et al.*, 1995; *Swenson and Gardner*, 1998; *Hickey and Yu*, 2005]. The relationship between the GW airglow intensity perturbation $I'/\overline{I}$ and the temperature perturbation $T'/\overline{T}$ at a particular altitude z is [*Liu and Swenson*, 2003]:

$$CF = \frac{\max(I'/\overline{I})}{\max(T'/\overline{T})}. \tag{5}$$

Figure 4 displays an analytic function of the cancellation factor (CF) with respect to λ_z:

$$\begin{aligned} &CF = 4.45\tanh(|\lambda_z|/15)^3 - 0.75 \ \text{ for } |\lambda_z| > 10\,\text{km, and} \\ &CF = (|\lambda_z|/10)^6 CF_{10} \ \text{ for } |\lambda_z| < 10\,\text{km,} \end{aligned} \tag{6}$$

where λ_z is in km, and CF_{10} is the value of CF at $|\lambda_z| = 10$ km. This function is designed to reproduce the features of the numerical calculation of the CF shown in Figure 9a of V09 (reproduced here as plus symbols) for very high-frequency GWs with $\tau = 10$ min. This function is used in the ray-trace model discussed in Section 4. Note that the numerical calculation of the CF by V09 is based on the model from *Liu and Swenson* [2003]; because it expresses the results in terms of λ_z (rather than the extrinsic phase speed), mean wind effects are therefore included. Such mean wind effects were shown to be quite important [*Hines and Tarasick*, 1987; *Hickey and Yu*, 2005], since GWs propagating against the mean wind have much larger $|\lambda_z|$ than those propagating in the same direction as the mean wind. We do not need to include the oscillations which occur in the CF for GWs with medium-scale λ_h and large phase speeds, however, because they are caused by the reflection of GWs in the thermosphere and the subsequent partial cancellation of the GW amplitudes within the OH layer [*Hickey and Yu*, 2005]; this is due to the assumption made by the full wave

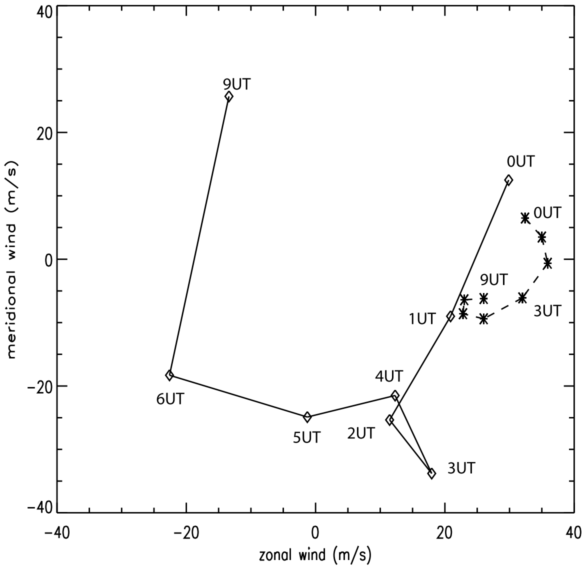

Figure 3. Hodograph wind at 88 km for 0000–0900 UT (data at 07 and 08 UT is absent) measured by the MF radar (solid line) and predicted by the TIME-GCM (dashed line).

model that the GW source is steady state and horizontally homogeneous. Because deep convective plumes are spatially and temporally localized, any GWs which reflect in the lower to mid thermosphere will propagate downward through the OH layer tens to hundreds of minutes and up to hundreds of km horizontally from the location where they initially propagated upwards through the OH layer; therefore, for a spatially and temporally localized GW source, there is no wave cancellation effect from reflected GWs within the OH layer above this source. Multiple plumes separated in time and space can lead to partial cancellations within the OH layer from reflected GWs; this effect, however, is included in our model.

[16] We note that estimating the OH airglow perturbations in this manner neglects OH perturbations that can arise from GWs with small λ_z which reach critical levels within the OH layer [*Hickey and Brown*, 2002]. This effect can affect those GWs propagating in the same direction as the background wind.

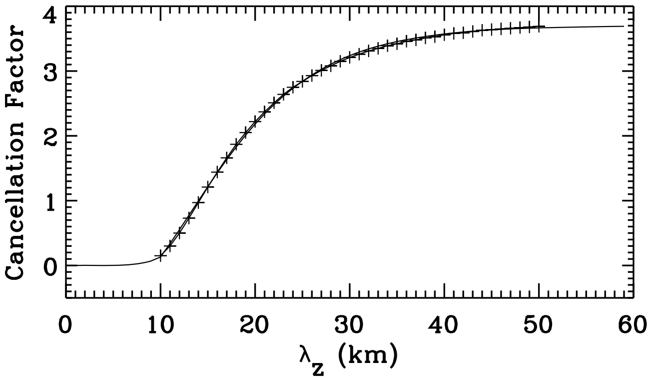

Figure 4. Analytic representation of CF (equation (6)) as a function of λ_z (solid line). Numerical calculation of the cancellation factor at the OH layer from V09 (plus symbols).

[17] The CF's are 0.13, 1.2 and 2.2 for GWs with $|\lambda_z| = 10$, 15 and 20 km, respectively. Therefore, the wave-induced perturbations in the airglow emission for the second and third group of GWs are approximately 15% and 120% of the corresponding temperature perturbations, respectively. This contributes to the result that the GWs in the second group are more difficult to see than those in the third group. The CF for the westward propagating GWs in the first group is approximately 3.5–3.7. This facilitates their easy observation if $T'/\overline{T}$ is relatively large. In Table 1, we summarize the apparent horizontal wavelength, period τ, phase velocity, vertical wavelength, propagation time, and cancellation factor for the GWs in groups 1, 2 and 3.

[18] Figure 5a shows the intensity perturbations, $I'/\overline{I}$, at 0300 UT. Here we calculate the intensity perturbations by subtracting off the background light first, similar to the procedure performed in V09. Then we subtract the average from each image and divide by the average to obtain the perturbations. At each pixel, the average is obtained 30 min prior to and 30 min after each image time, with a 1 h running window. Figures 5b, 5c, and 5d show the intensity perturbations at 102.7W, 39.5N and 104.0W, respectively. The latitude and longitude ranges in Figures 5b, 5c and 5d are chosen to highlight the GWs from group 1, group 1 and group 3, respectively. For each line plot, the average value over the plotted interval has been subtracted off. The group 2 GWs are difficult to see at 105.0W and 40.5N because of noise in the images. For Figures 5b and 5c, the line plots are approximately perpendicular to the wave phase fronts of the group 1 GWs. Figures 5b and 5c clearly show periodic oscillations with estimated horizontal GW wavelengths of $\lambda_h \sim 30$ km at this radius. Figure 5d shows relatively periodic oscillations with a 35 km spacing, although there is some noise and interference from other waves. Note that this 35 km spacing is larger than group 3 GW's $\lambda_h \sim (26–30) \pm 4$ km, because the slice is not perpendicular to the wave phase front.

[19] From Figures 5b–5d, we estimate $I'/\overline{I}$ at 0300 UT for the first and third group of GWs to be ~5–8% and ~3–4%, respectively. Using λ_z calculated above and the CFs from Figure 4, we estimate temperature perturbation amplitudes of $T'/\overline{T} \sim 1.4–2.3\%$ and $T'/\overline{T} \sim 2.5–3.3\%$ for the first and third group of GWs, respectively. These values are consistent with the temperature and intensity perturbations obtained from the single convective plumes on 11 May 2004 (see Figures 1c and 10h of V09).

[20] GW structures in the images evolved dramatically over the night. GWs from the second group cannot be seen in Figure 2b. On the other hand, full rings of convective GWs in Colorado were clearly visible after clouds moved out of the field of view (FOV). Interference of wave patterns is evident between concentric GWs from different sources.

Table 1. The Apparent Horizontal Wavelength, Period, Phase Velocity, Vertical Wavelength, Propagation Time and Cancellation Factor for the GWs in Groups 1, 2 and 3

Group	λ_h (km)	τ (min)	c_h (m/s)	λ_z (km)	Δt (min)	CF
GW 1	26–30 ± 4	8 ± 1	60 ± 20	37–53 ± 15	20–38 ± 15	3.5–3.7
GW 2	20 ± 4	10 ± 1	34 ± 10	11 ± 3	96 ± 29	0.15
GW 3	26–30 ± 4	10 ± 1	45 ± 15	15 ± 5	75 ± 28	1.2

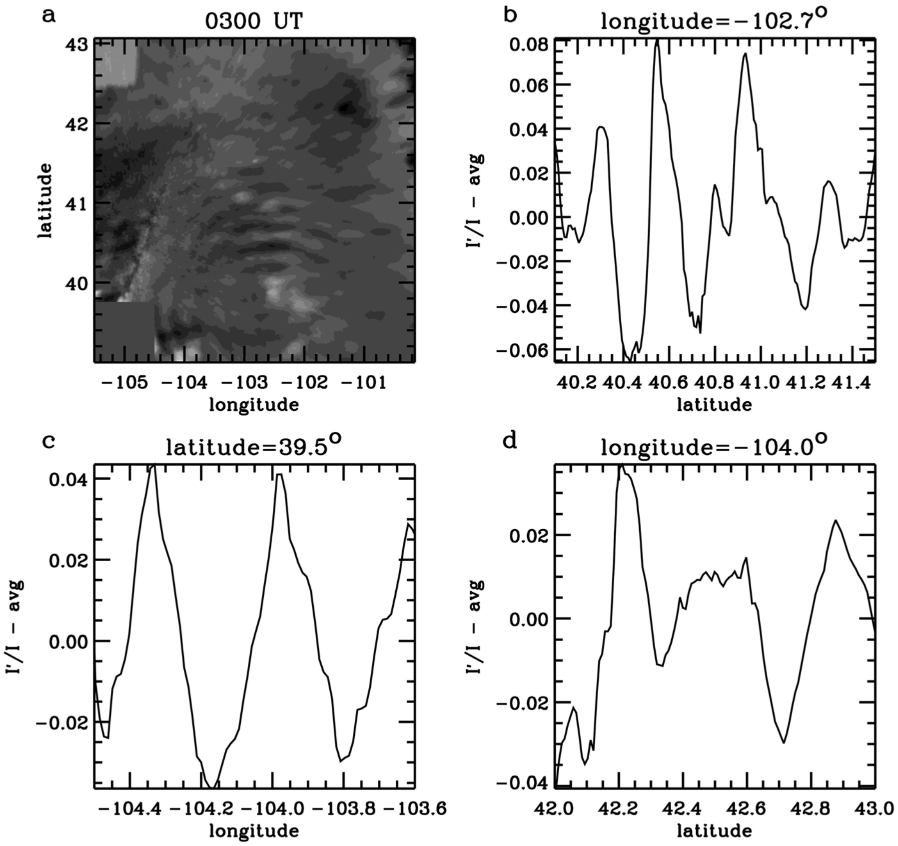

Figure 5. OH intensity perturbations at 0300 UT. (a) $I'/\overline{I}$ image. The intensity perturbations west of 104.5°W and south of 39.75°N are set to zero because of the presence of bright clouds. (b) $I'/\overline{I}$ at longitude = −102.7°. (c) $I'/\overline{I}$ at latitude = 39.5°. (d) $I'/\overline{I}$ at longitude = −104.0°. The averages are subtracted in Figures 5b–5d.

Moreover, at 0354 UT (Figure 2c), there are multiple groups of northwestern propagating GWs from the epicenters near (39N, 102W). Their wavefronts overlay on and interfere with each other, making it difficult to measure the wavelengths accurately at this time. For example, there are several groups of adherent wavefronts near (40N, 103W), (40N, 104W) and (41N, 105W). These wave patches show larger scales with increasing radii. Qualitatively, this is in agreement with the GW dispersion relation with constant Δz and Δt and m ∼ $k_h R/\Delta z$ [Y09, equation (4)]

$$\lambda_h = \frac{2\pi R^2 (1 + \Delta z^2/R^2)^{3/2}}{N \Delta z \Delta t}. \tag{7}$$

Clouds moved in around 0430 UT and only arcs (a quarter of a full ring) can be seen in the images. The averaged horizontal wavelength for the northwestward propagating GWs from group 1 with radii of 250–280 km decreases from 25 ± 2 km at 0530 UT (Figure 2f) to 22 ± 2 km at 0602 UT (Figure 2g), and finally to 18 ± 2 km at 0702 UT (Figure 2i). Because the GWs with the same periods (or radius R) and shorter horizontal wavelengths have smaller vertical group velocities c_{gz} (see equation (4)), these more slowly propagating GWs reach the airglow layer at a later time (i.e., larger Δt from equation (7)). Therefore, the horizontal wavelength of the GWs at the same radii from the same source decreases with time. Assuming these GWs were all excited by the same convective source at 0214 UT in Colorado, Figure 6 shows the theoretical relationship between λ_h and Δt with R ∼ 250 km and 280 km. We find that Δt is 196 min, 228 min and 288 min at these three different times. The observed λ_h's are in good agreement with the GW dispersion relation if these GWs were excited by a convective object around 0214 UT. The convective sources of these GWs will be discussed in the next section.

[21] Figure 7 shows the OH intensity perturbations at 0800 UT at 104 W. We see that the OH perturbations created by these GWs are ∼2–3%. After 0800 UT, only the third group of GWs propagating SWward can be clearly observed. Because the wave patterns from different plumes interfere with each other, it is difficult to determine their horizontal wavelengths later in the night (Figures 2j–2l). The apparent phase speed is in the range of ∼75–100 m/s. The imager FOV was completely blocked by clouds in the images after 0845 UT, indicating the end of the observations. Note that in Figure 2l, other groups of concentric arc-like GWs propagated northward and eastward; these waves are denoted by the green and blue arrows, respectively. These GWs were obviously excited by different sources other than those of the aforementioned three groups of GWs. Because those GWs can only be identified in a few images around 0830 UT, they will not be discussed in detail in this paper. From 0300 to 0845 UT, an unprecedented total of 6.75 h of concentric GWs were observed; this is therefore the longest recorded

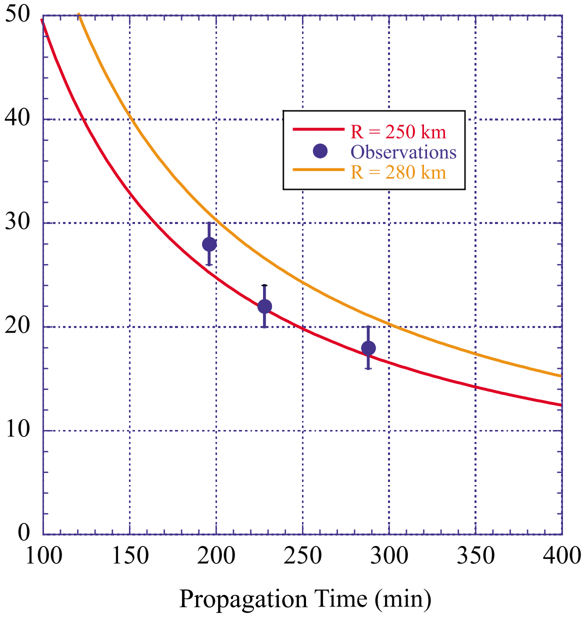

Figure 6. Horizontal wavelength in km (y axis) as a function of the propagation time. Radii of 250 km (red line) and 280 km (orange line) as a function of time, assuming the GWs were launched at 0214 UT, calculated from equation (7). The three dots from left to right denote observed horizontal wavelengths at 0530, 0602 and 0702 UT.

occurrence of convectively generated concentric GWs at this height of 87 km.

3. Satellite, Radar and Hail Observations of Convective Plumes

[22] Y09 showed that there was deep convection near the epicenter of the concentric GWs approximately one hour before the observations. This includes the event on 8 September 2005 (see Figure 4 of Y09). In this paper, using extensive satellite, weather radar and hail observations, we search for the sources of the aforementioned three groups of GWs.

[23] The GOES satellites are geosynchronous and play a key role in U.S. weather monitoring and forecasting. GOES IR satellite images were available every 15–50 min on the night of 8 September 2005. An example is shown in Figure 8a at 0155 UT. The thunderstorm system near the epicenter of the GWs from group 1, 2 and 3, in Colorado, Nebraska and South Dakota is labeled storm 1, 2 and 3, respectively. Besides these three large thunderstorm systems, other cumulous clouds and anvils are observed in southern Colorado, New Mexico and northern Texas. Since convective plumes overshoot the tropopause adiabatically, they appear as a few or more colder pixels to the infrared satellite sensor. By manipulating the IR images graphically, it is possible to determine the temperature of the anvil cloud, which is created from old convective plume material located at the tropopause. The groupings of colder pixels surrounded by warmer anvil are likely convectively overshooting cloud material (most likely ice crystals) [*Vadas and Liu*, 2009; *Vadas and Crowley*, 2010].

[24] A full list of plumes, clusters, and complexes which overshot the tropopause over the Great Plain from 0110 to 0730 UT on 8 September 2005 was compiled using the GOES IR images and the technique described above. This list was composed only of plumes with updraft velocities > = 10 m/s. A cluster contains 2–4 loosely spaced, non-interacting plumes. A complex contains 2–4 closely spaced, interacting plumes. If there was more than 25 min separating the images, the locations of the plumes at the intervening times (every 15–20 min) were taken to be that from the prior image. This is because an established updraft will repeatedly send up pulses of buoyant air provided that sufficient Convective Available Potential Energy (CAPE) is available. A convective plume moves upward and overshoots the tropopause, then collapses. The collapse brings cooler air to the surface, which then can spread into a nearby region of high CAPE, and trigger the formation of (a) new convective plume(s). The tropopause altitudes are determined from 3-hourly global reanalysis data of the height field (~15–16 km on 8 September 2005). The (maximum) updraft velocities are obtained from 3-hourly CAPE maps (from the NCDC NOMADS site):

$$w \sim \sqrt{2 \cdot CAPE}. \tag{8}$$

Because the amplitudes of the GWs excited by a convective plume are proportional to that plume's updraft velocity,

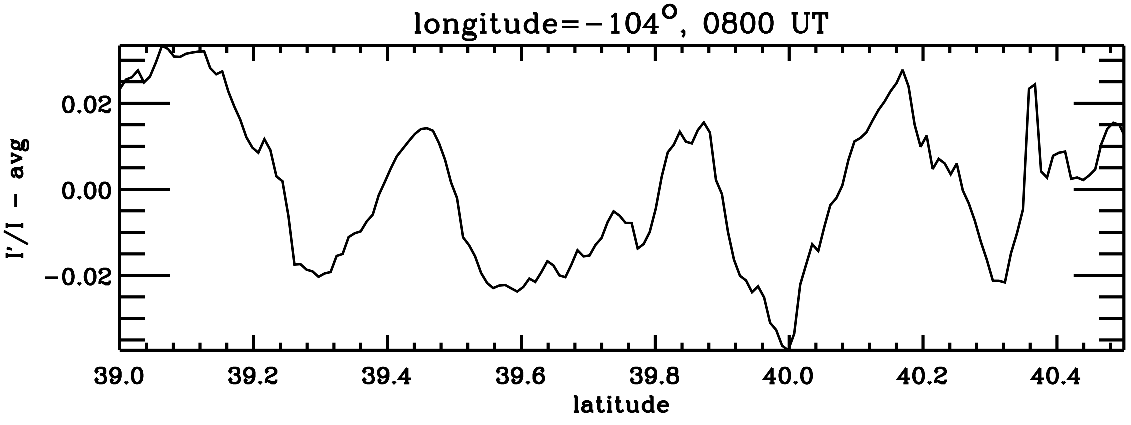

Figure 7. OH intensity perturbations at 0800 UT at 104 W. The average is subtracted.

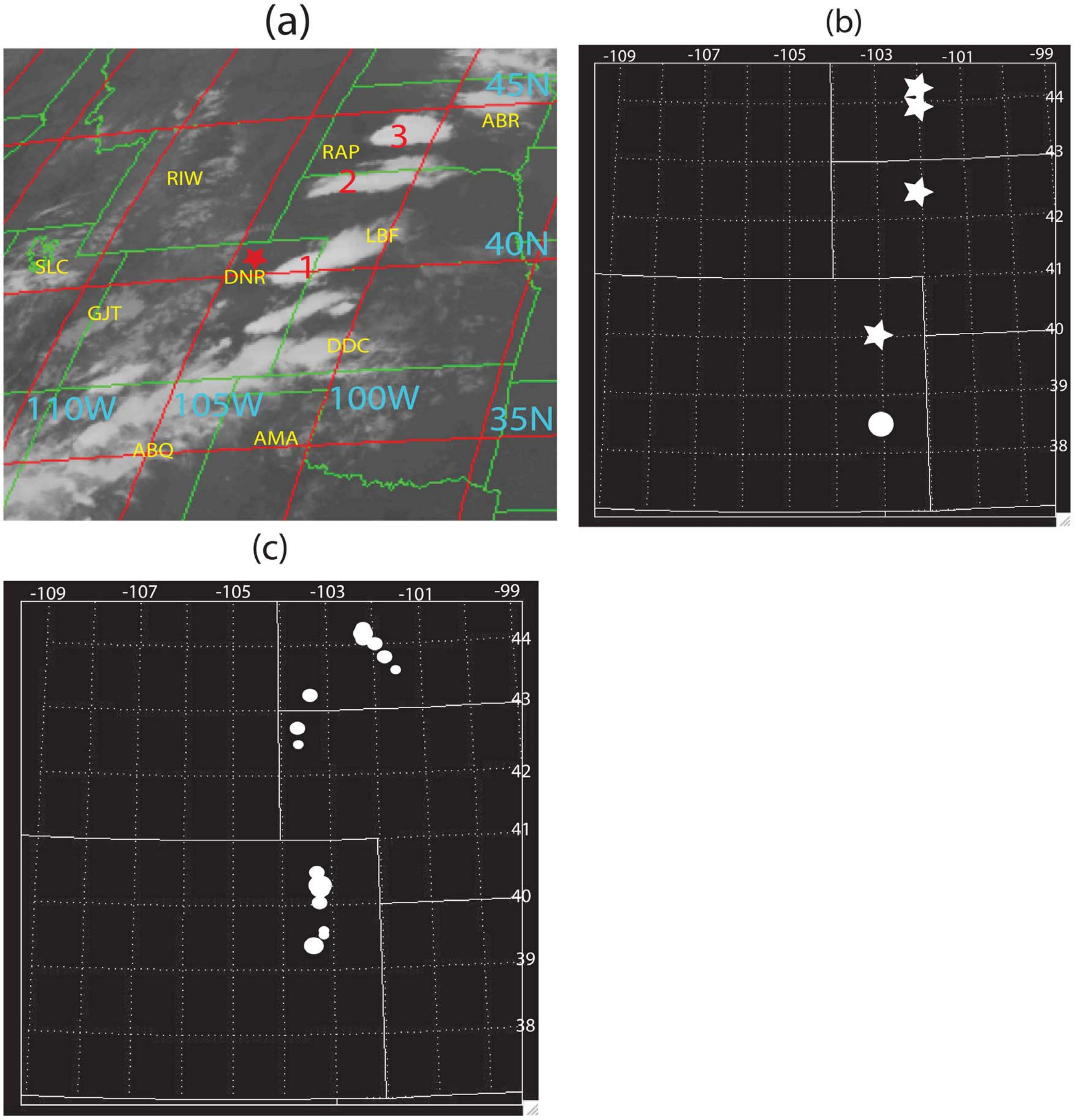

Figure 8. (a) GOES satellite image at 0155 UT on 08 September 2005. The red star indicates the location of YRFS. Cumulous clouds associated with Thunderstorms 1, 2 and 3 are numbered accordingly. The radiosonde stations are shown as yellow letters. (b) The distribution of plumes that had strong updraft (>40 m/s) at 0155 UT. The white dot denotes a single plume, and the stars denote clusters. (c) The distribution of hail (white dots) reported on 8 Sep. 2005. The sizes of the hail (0.75″, 1″, 1.75″ and 3″) are indicated by the area of the white dots.

the plumes with the largest updraft velocities produce the largest-amplitude GWs. Altogether, 236 single plumes, clusters and complexes were identified.

[25] At 0155 UT (shown in Figure 8a), the largest convective plumes had updraft velocities of 70 m/s. For only the strongest plumes with updraft velocities >40 m/s, 5 convective objects were identified, as illustrated in Figure 8b. Two were clusters in southwestern South Dakota (44–45N and 102W), one was a cluster in western Nebraska (at 42.5N and 102W), one was a cluster in northeastern Colorado (at 40N and 103W), and one was a single plume in eastern Colorado (at 38.5N and 103W). The rest of the updrafts in southern Colorado and New Mexico resulted from weaker single plumes and clusters. Comparing Figure 2a and Figure 8b, the clusters in South Dakota and northeastern Colorado coincide geographically with the epicenters of the GWs from the 1st and 3rd group. The cluster in Nebraska is to the east of the epicenter of the GWs from the 2nd group. Recall that the GWs from the 1st, 2nd and 3rd group are estimated to be excited at 0205–0255 UT, 0100–0155 UT and 0120–0215 UT. Therefore, the 3nd group of GWs at ~0300 UT were very likely excited by the clusters in South Dakota at 0155 UT, while the 1st and 2nd group of GWs were likely excited by clusters in Colorado and Nebraska after and before 0155 UT, respectively. This explains why the cluster in Nebraska at 0155 UT is east of the GW epicenter at 0300 UT, given the fact that the storm moved eastward.

[26] The National Weather Service NEXRAD radar map can be used to support the GOES observations of convective plumes and clusters. Figure 9a shows the radar reflectivity map at 0152 UT on 8 September 2005, from the NEXRAD radar located at North Platte, Nebraska (41N, 100W), plotted with the NOAA Weather and Climate Toolkit. Like Figure 8a, the high reflectivities in Figure 9 associated with thunderstorm systems in northeastern Colorado (40N, 103W), western Nebraska (42N, 103W) and South Dakota (44N, 102W) are also labeled 1, 2, and 3. By comparing to Figure 8a, we see that the shapes of the cumulous clouds and anvils resemble that of strong reflectivities reasonably well. The locations of strong reflectivity coincide with the clusters indentified in the satellite images, as well as with the GW epicenters. Figure 9b shows the reflectivity map at 0153 UT from the radar station in southern Colorado at Pueblo (38N, 104W). Along with storm 1, strong reflectivity is seen in eastern Colorado (38.5N, 103W), which coincides with the single plume identified in satellite image in eastern Colorado. Weaker reflectivities are distributed in southern Colorado and northern New Mexico.

[27] To identify the convective overshooting, we search for strong reflectivities (>18.5 dBZ) above the tropopause (15–16 km). Because each NEXRAD radar has a limited number of elevation angles, the vertical resolution of the reflectivity is low a large distance from the radar. For example, 150 km away from the radar at Pueblo, CO, the reflectivities near the tropopause are measured at $z = 13$ km, 15.5 km and 18 km. Therefore, we may miss some of the overshooting from the NEXRAD radar maps when the storms are far from the radar. This is why the satellite images are more useful for this task, even though the reflectivity maps are obtained every 4–6 min. Table 2 lists the estimated locations and times when plumes overshot the tropopause by >1 km between 0 and 3 UT, determined from the radar map. We see that the strongest clusters identified from the satellite images at 0155 UT are also seen by the radar. As mentioned previously, the collapse of a convective plume can trigger the formation of one or more new convective plumes, if the storm system has large CAPE on the outskirts of the old plume. Thus for a typical plume (maximum) updraft velocity of 40–50 m/s (average updraft velocity of 20–25 m/s), we estimate the time for each plume to reach the tropopause (after moving upward ~10 km) to be ~6–8 min. Detailed modeling and comparison with the observed GWs led to an estimated plume duration of 10 min [V09]. From Table 2, we find that each "child" convective plume occurs ~15–20 min later than the "parent" plume. Additionally, from Table 2, the satellite-identified clusters at 0155 UT in southwestern South Dakota (44–45N and 102W), in western Nebraska (at 42.5N and 102W), in northeastern Colorado (at 40N and 103W) are identified in the radars at 0142/0214 UT, 0130 UT and 0145 UT, respectively. Thus, the plume observations from the GOES and the NEXRAD radars are in good agreement. We note that the overshooting plume at 0214 UT supports the assumption of the convective source in Figure 6.

[28] Another well-known severe weather phenomenon on the Great Plain is hail, which can form from strong updrafts of moist air within a thunderstorm. Thus, hail and concentric GWs share similar generating mechanisms, except that hail may or may not be produced. All plumes create arc-like GWs; however, such arc-like patterns are typically disrupted by large winds in the stratosphere and mesosphere, which instead create the appearance of planar, linear waves in airglow images. On the night of 8 September 2005, a handful of hail events were reported; the record can be found at NOAA's Storm Prediction Center (http://www.spc.noaa.gov/climo/index.html). The hail sizes range from 0.75″ to 3″. (The National Weather Service (NWS) issued severe thunderstorm warnings whenever a thunderstorm produces hail larger than 3/4″ diameter.) The updraft velocities needed to create 0.75″, 1.5″ and 3″ hail are 25, 35 and >40 m/s [*Renick and Maxwell*, 1977]. Figure 8c shows the locations and sizes of the reported hail between 0 and 9 UT from the three thunderstorms in Colorado, Nebraska and South Dakota. Comparing Table 2 and Figures 8a–8c, the locations of the hail throughout the night qualitatively agree with the locations of the convective overshoots at 0155 UT.

[29] Strong updrafts and hailstorms in Nebraska (Storm 2) ceased after 2 UT, and those in northeastern Colorado (Storm 1) ended after 5 UT. On the other hand, thunderstorm 3 in South Dakota produced hailstorms and strong convective plumes throughout the night. During this time, the whole storm system traveled eastward. As shown in Figure 9c, only strong reflectivities associated with Storm 3 can be detected by the NEXRAD radar at 0600 UT. Additionally, Storm 3 traveled eastward ~500 km over 4 h; this is an average speed of ~30 m/s. Other than the storm systems in South Dakota, weaker single plumes and complexes were identified in southern Colorado and New Mexico during the latter part of the night. These convective plumes are likely the sources of the concentric GWs denoted by green and blue arrows in Figure 2l.

[30] In this section, we demonstrated that different convective sources excite concentric GWs. This result shows that the mesoscale dynamics in the mesopause region is influenced by the meteorological activities and extreme weather occurring in the troposphere. Convective GWs propagated to the mesosphere after tens of minutes or hours after the convective overshooting. In general, nearly all of the GWs can be traced back to their sources, in terms of geographical matching between the epicenters and the plumes/clusters, and the propagation times. This provides us with a classic example of the coupling of the lower and middle atmospheres by GWs. These observations also yield a unique opportunity to test GW excitation and ray-trace models. In the next section, we will use such GW excitation and ray-trace models to simulate the excitation and propagation of convective GWs when multiple convective sources are occurring concurrently.

4. Modeling the OH Perturbations From Gravity Waves Excited by Convective Sources

[31] Over the past few decades, many numerical models have been developed to simulate the GWs excited by deep convection [e.g., *Holton and Alexander*, 1999; *Pandya and Alexander*, 1999; *Horinouchi et al.*, 2002; *Lane et al.*, 2003]. It is generally believed that there are two GW sources within a convective system: diabatic forcing (i.e., latent heating and cooling), and nonlinear forcing from the movements and perturbations within a convective system (i.e., the divergences of the momentum and heat fluxes) [*Lane et al.*, 2001]. Both sources are important in full,

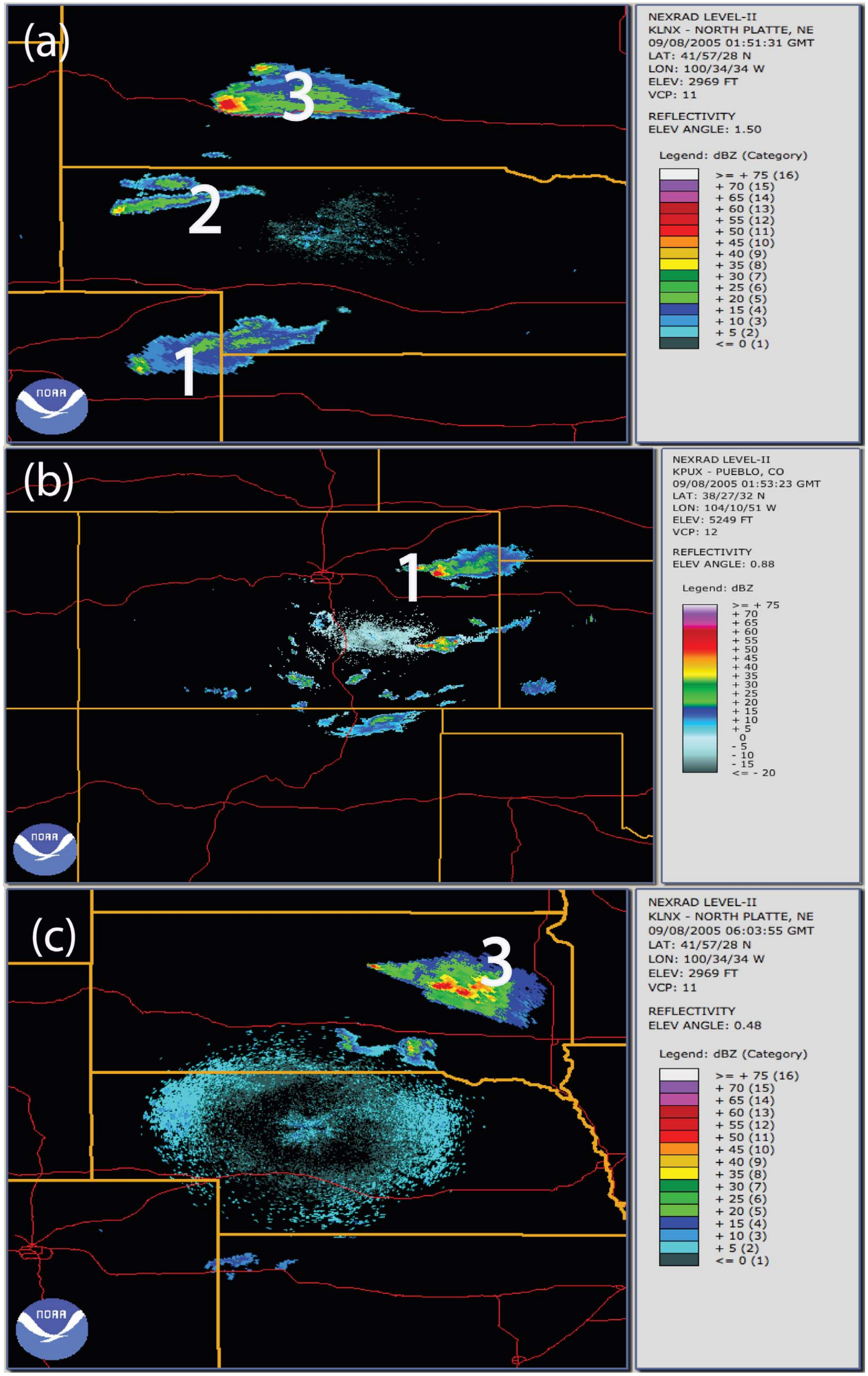

Figure 9. NEXRAD reflectivity charts (a) at 0152 UT from North Platte, NE, (b) at 0153 UT from Pueblo, CO, and (c) at 0603 UT from North Platte, NE, on 8 September 2005. Thunderstorm systems in northeastern Colorado, western Nebraska and South Dakota are tagged Thunderstorm 1, 2 and 3, respectively. The color bar is the radar reflectivity. The green, yellow and red colors indicate regions of convection and precipitation.

Table 2. Times and Locations of Some Overshooting Events Before 3 UT in Colorado (Thunderstorm 1), Nebraska (Thunderstorm 2) and South Dakota (Thunderstorm 3) Determined From the NEXRAD Radar Map

	Thunderstorm								
	1	1	1	1	2	2	3	3	3
UT	0033	0112	0142	0214	0010	0130	0117	0145	0235
Long (W)	103.1	103.1	103.1	103	103.6	103.4	102.1	102.1	101.8
Lat (N)	40.1	39.9	39.8	39.7	42.7	42.4	44.1	44.1	43.8

nonlinear, moist, cloud-resolving simulations, and result in GWs with similar amplitudes, scales, and periods [*Song et al.*, 2003; *Choi et al.*, 2007]. This lends credence to the idea that either dry source, by itself, can be used to model the GWs excited by convection. However, these two sources are largely out of phase with one another; if only a single source (say diabatic forcing) is used to model the excitation of GWs in a dry-air simulation (as is commonly done), the GW amplitudes are ~2 times larger than the GWs in the nonlinear, moist simulation [*Song et al.*, 2003; *Choi et al.*, 2007]. However, if both dry GW sources are included, then realistic GW amplitudes and similar GW spectral characteristics are obtained. A new GW parameterization modifies the diabatic forcing to include this nonlinear forcing [*Chun et al.*, 2008]. *Choi et al.* [2007, Figure 5] showed that the shape of the GW spectra from the dry diabatic or nonlinear forcing are quite similar to that of the moist simulations for simple unsheared cells for horizontal phase speeds greater than ~20–25 m/s; the amplitudes, however, were still ~2 times too large. Therefore, linear dry GW excitation models which include only one of these sources must reduce the GW amplitudes accordingly, even for large phase speeds.

[32] In the literature, there are "dry-air" linear models which describe this excitation process as a diabatic forcing [e.g., *Alexander et al.*, 1995; *Piani et al.*, 2000; *Walterscheid et al.*, 2001; *Beres*, 2004], while others as an overshooting of the convective plumes into the stratosphere [*Stull*, 1976; *Vadas and Fritts*, 2009]. GW excitation from deep convection excites high frequency GWs with $\lambda_h \sim 1$ km to hundreds of km, and with periods of 5 min to a few hours.

[33] Our GW source model is an idealized model which implements the latter process [*Vadas and Fritts*, 2009]. This model implements the analytic, Boussinesq solutions for the generation of GWs from an "envelope" of upward-moving air in a simple, unsheared background wind, and was recently modified to include compressibility (S. L. Vadas, manuscript in preparation, 2012). Because not all of the air is upward-moving within this envelope, we multiply the GW amplitudes by a fill factor which is < = 1. We also multiply each GW's amplitude by 1/2 in order to compensate for its overestimation from the neglect of diabatic forcing (see above) [*Song et al.*, 2003; *Choi et al.*, 2007]. This model neglects the larger-amplitude, small-scale GWs with $\lambda_h < 10$ km, $\lambda_z < 10$ km, and small phase speeds excited by the smaller-scale processes associated with the convective updrafts and wind shear [e.g., *Lin and Chun*, 1991; *Lane et al.*, 2003]. Because we are neglecting the smaller-scale GWs which have phase speeds <20–30 m/s and can greatly affect the dynamics of the stratosphere, and because the excited GWs are ray traced from a single point in space and time (i.e., a point source approximation), these models are not appropriate for GW studies in the stratosphere. Note that the GWs which reach the mesopause region typically have phase speeds >20 m/s, thereby ensuring that the GW spectrum which arises from our vertical body force model can be scaled by a constant factor. Note that by neglecting these smaller-scale GWs, we are also neglecting any secondary GWs which may be excited when these GWs break. We argue in Section 4 why we are likely only observing the primary, not secondary, convectively generated GWs.

[34] We model here the GWs excited by the 236 single plumes, clusters, and complexes, identified from the GOES satellite images, as discussed in the previous section. We model a plume as a vertical body force with a diameter of $D_H = 5$ to 20 km, which lasts for the duration σ_t. We model a cluster and a complex as 3 identical plumes at the corners of an equilateral triangle. The distance between adjacent plume centers is 3 D_H for a cluster, and 2.25 D_H for a complex. These average separation distances are determined from the GOES IR satellite images. We separate the plume start times in the clusters and complexes by $\sigma_t/2$. Via comparison with OH airglow observations on 11 May 2004 of concentric GWs with $\lambda_h \sim 20$–100 km and $\tau \sim 5$–15 min from 2 nearly simultaneous plumes, it was found that $\sigma_t = 10$ min and a fill factor of 0.5–0.75 fit the data well [V09]. Here, we assume $\sigma_t = 10$ min and a fill factor of 0.5 for all single plumes.

[35] While this fill factor works well for a single plume, it results in GW amplitudes that are ~10 times too large for GWs ray traced from clusters and complexes. We explain the needed reduction for clusters and complexes in our ray trace model as follows. We first multiply an excited GW's amplitude by 1/3 to account for the non-localization of the plumes within the cluster or complex (since the GWs are ray traced from a single location in the ray-trace model). We then multiply this amplitude by 1/3 to account for the non-simultaneity of the plumes (since all GWs are ray traced from a single time in the ray trace model). Combining these factors, we estimate a total reduction of 1/9 = 0.11 for GWs ray traced from clusters and complexes in our ray trace model. In this paper, we will compare the intensity perturbations from storm 1 (which is a cluster) from Figure 2 with our model results at 0300 and 0800 UT (see later in this section), and we find that they agree reasonably well if the total multiplying factor is 0.1, in agreement with our estimate. We use this same factor for a complex, as it contains the same number of plumes, and so results in the same 1/9 factor from the non-localization and non-simultaneity of these plumes.

[36] Two million GW packets are created by each plume/cluster/complex in our model, and are inserted into a non-hydrostatic and compressible ray-trace model [*Vadas and Fritts*, 2009]. The GWs excited by these convective objects are then ray-traced from a single location and time to z = 110 km. The ray tracing is performed using both model and zero winds. The zero wind results are necessary in order to distinguish between background wind effects and the non-uniformity of the GW spectral amplitudes (since the amplitude of each GW depends on its wavelength, frequency, and propagation speed). This is especially important here, because we integrate these GWs up to 8 h after their excitation in order to capture the late-time effects created by the

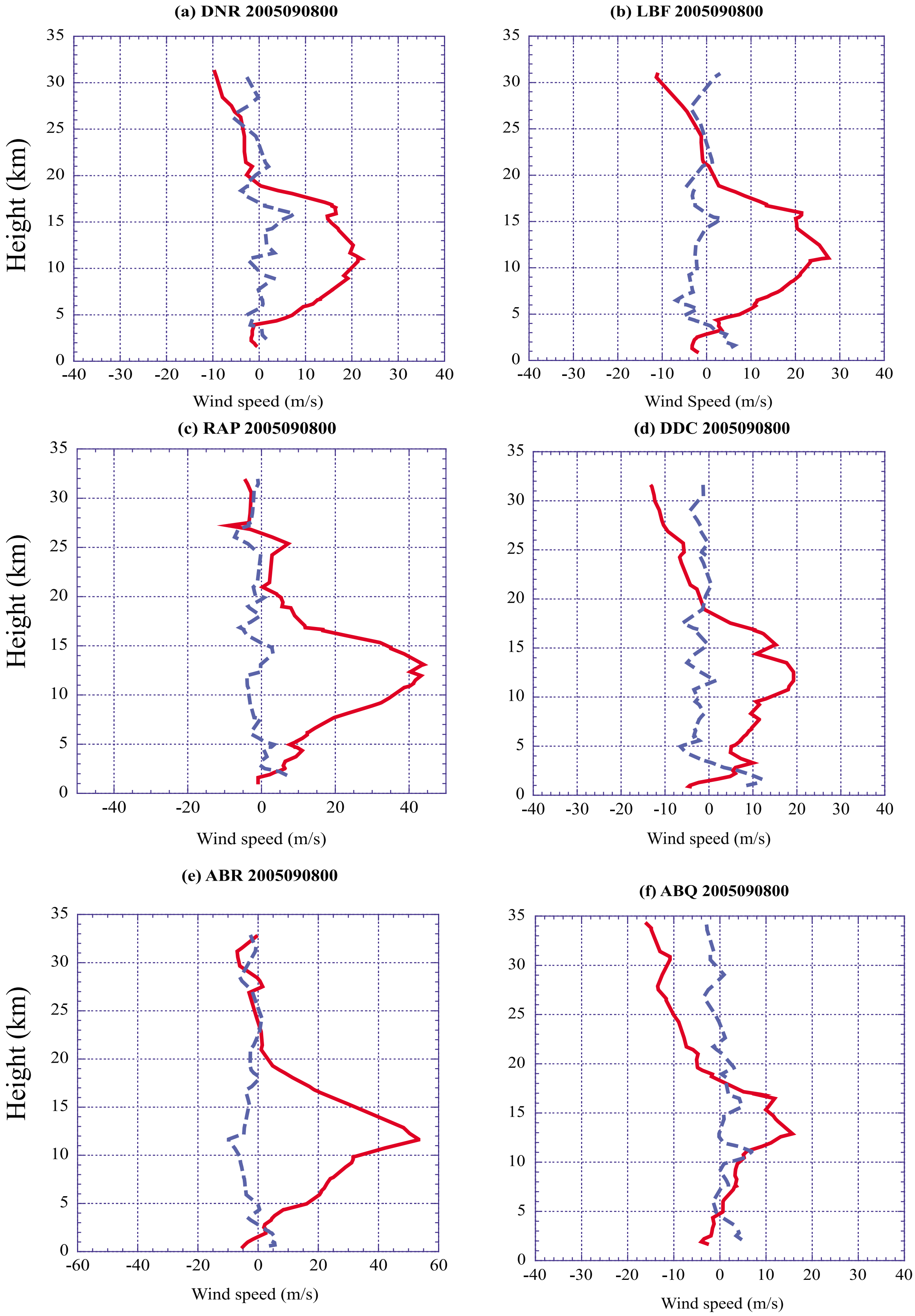

Figure 10. Radiosonde zonal (solid line) and meridional (dashed line) wind at 00 UT on 08 September 2005, measured at the stations of (a) Denver (39.75N, 104.87W), (b) North Platte (41.13N, 100.68W), (c) Rapid City (44.08N, 103.21W), (d) Dodge City (37.77N, 99.97W), (e) Aberdeen (45.45N, 98.43W), and (f) Albuquerque (35.05N, 106.61W).

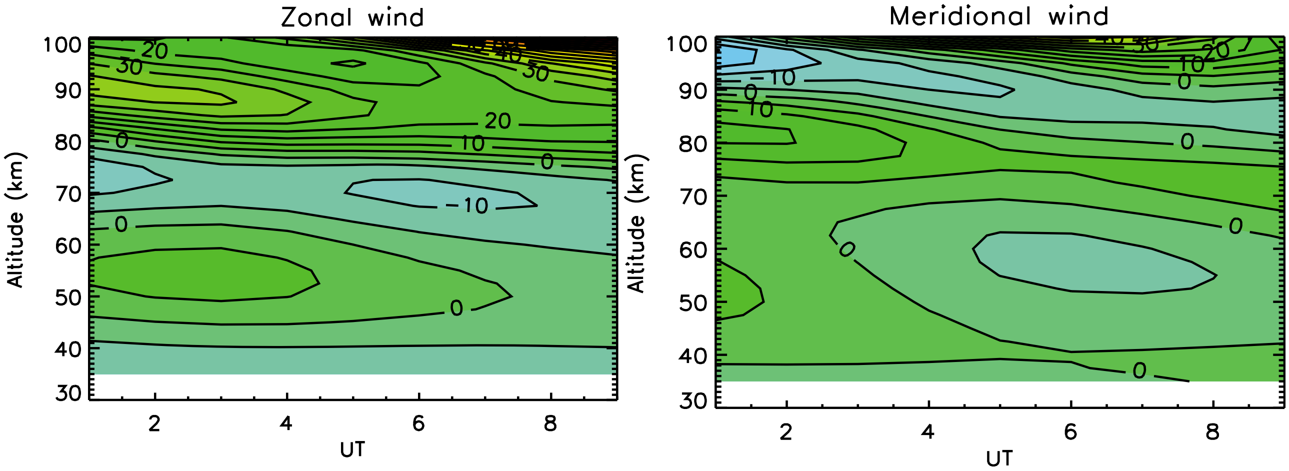

Figure 11. Horizontal winds near YRFS on 08 September 2005 from the TIME-GCM.

small-scale, slowly propagating GWs, whereas past mesopause studies have only integrated these GWs (through zero winds) for a few hours after excitation [*Vadas and Fritts*, 2009]. The zero wind results also provide an understanding of the sensitivity of our results to the background wind; this is important, because the TIME-GCM model winds may not provide an entirely accurate depiction of the actual winds that evening. We save the momentum fluxes in (x, y, z, t) bins in a 872 km × 872 km horizontal region centered on Yucca Ridge. The bin sizes are 6 km × 6 km × 3 km × 4 min in x, y, z and t, respectively. After ray-tracing the GWs from a convective object, the temperature perturbations $T'/\overline{T}$ are reconstructed at z = 86 km [V09]. We then convert these perturbations to approximate intensity perturbations, $I'/\overline{I}$, via equations (5) and (6) for better comparison with the imager observations. We do not include the phase shift between $I'/\overline{I}$ and $T'/\overline{T}$ [*Liu and Swenson*, 2003], because the exact start times of the convective objects are uncertain by ~15 min or more (because the GOES images are only available every 15–50 min).

[37] The ray-trace model includes the effects of parameterized GW breaking via Lindzen's saturation condition [*Lindzen*, 1981]. This is accomplished by ray-tracing all GWs a second time, and reducing their amplitudes when they reach bins where the sum of the non-dimensional GW amplitudes squared (from the first run) is greater than one [*Smith et al.*, 1987]. (We note that at all times, there are regions in our simulated volume for which the non-dimensional amplitudes are >1 during the first run.) We are not including secondary GWs excited by the momentum deposition from wave breaking here, because these GWs have much smaller amplitudes relative to the primary breaking GWs in 3D simulations [*Vadas et al.*, 2003]. These secondary GWs also have horizontally asymmetric concentric ring phase lines in 3D simulations [*Vadas et al.*, 2003], which is not observed here (see Figure 2). Finally, this model also includes the change in the observed frequency from time-varying background winds [*Eckermann and Marks*, 1996].

[38] Our wind and temperature model is composed of balloon soundings at 0 UT from the ground to 30–35 km from various stations across the Great Plain (downloaded from Department of Atmospheric Science, University of Wyoming, http://weather.uwyo.edu/upperair/sounding.html). The radiosonde wind profiles near the thunderstorms are shown in Figure 10. The locations of these stations are marked in Figure 8a. The meridional winds are quite weak below 35 km. The zonal winds are eastward with 10–30 m/s magnitude near the tropopause (z ~ 15 km). The wind shears are <6 m/s/km. We note that the direction and magnitude of the tropospheric wind is in agreement with the motion of the storms. From 35 km to 150 km, we obtain hourly wind and temperature from the high-resolution TIME-GCM with 2.5° horizontal resolution. The lower boundary of the TIME-GCM is specified by the European Centre for Medium-Range Weather Forecasts (ECMWF) reanalysis data at 10 hPa, and is updated every 6 h. A detailed description of the TIME-GCM is provided by *Roble and Ridley* [1994]. The TIME-GCM zonal and meridional winds near YRFS on 08 September 2005 are shown in Figure 11. Since the zonal mean zonal wind switches direction in September, the total background horizontal wind velocity is small at that time (<10 m/s) [Y09]. Superposed on the mean wind, the downward progression of thermal tides is apparent. The overall tidal amplitude is less than 20 m/s below the airglow layer. Comparing the TIME-GCM wind to the MF radar wind at 88 km in Figure 3, the TIME-GCM wind is always eastward throughout the night while the MF radar wind varies dramatically.

[39] Figures 12 and 13 shows horizontal slices of the calculated OH airglow intensity perturbations $I'/\overline{I}$ from 0300 to 0830 UT on 08 September 2005 in the same time sequence as in Figure 2. Here, the GWs are ray-traced through the model (TIME-GCM/radiosonde) and zero background winds, respectively. The model wind results show distorted and partial concentric ring patterns of GWs from wind filtering [V09], while the zero-wind results show symmetric, concentric rings. Altogether, the agreement between the model wind results and the observations is quite good. Figures 12a–12c and 13a–13c show wave interference patterns in Colorado at 104W and 40N, similar to those in Figures 2a–2c. At early times, when the fast excited GWs reach the OH layer, the model and zero wind results are similar. This is due to the fact that these early GWs have large horizontal phase speeds, and are not significantly

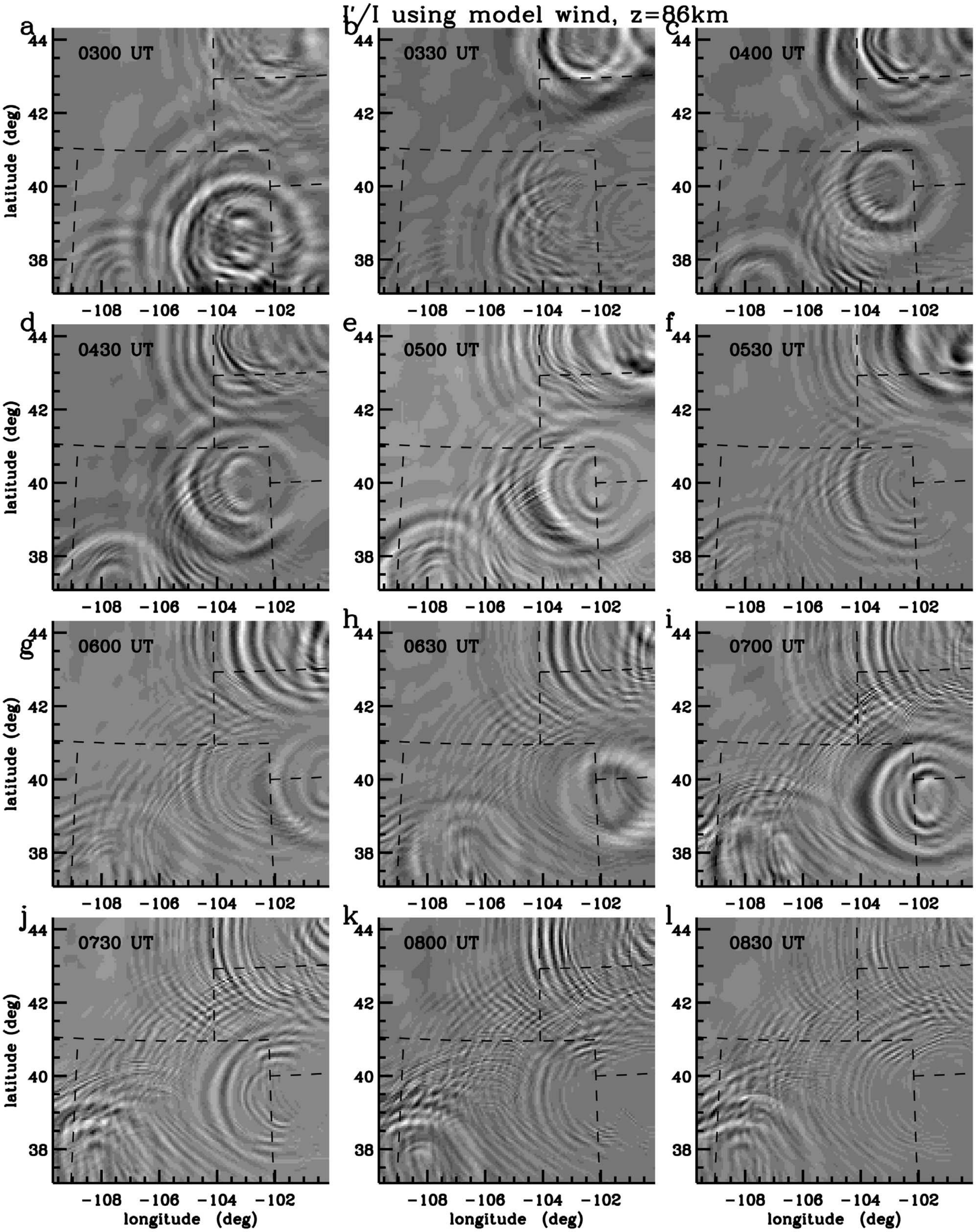

Figure 12. Horizontal slices of $I'/\bar{I}$ at z = 86 km at 0300, 0330, 0400, 0430, 0500, 0530, 0600, 0630, 0700, 0730, 0800 and 0830 UT, calculated from the ray trace model on 08 September 2005. The background wind model with the radiosonde/TIME-GCM wind is used. The dashed lines show the state lines.

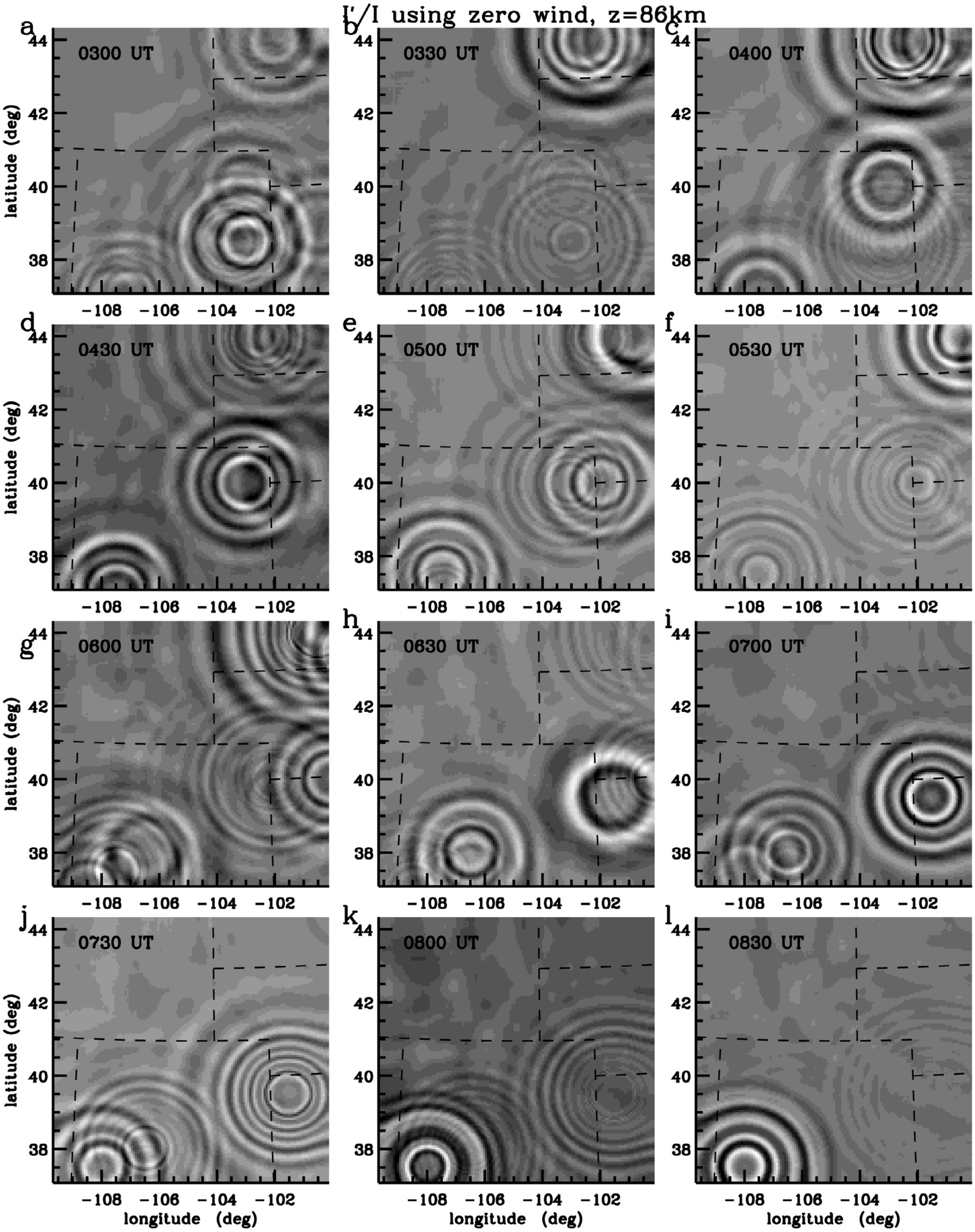

Figure 13. Horizontal slices of $I'/\bar{I}$ at z = 86 km at 0300, 0330, 0400, 0430, 0500, 0530, 0600, 0630, 0700, 0730, 0800 and 0830 UT, calculated with a zero background wind in the ray trace model. The dashed lines show the state lines.

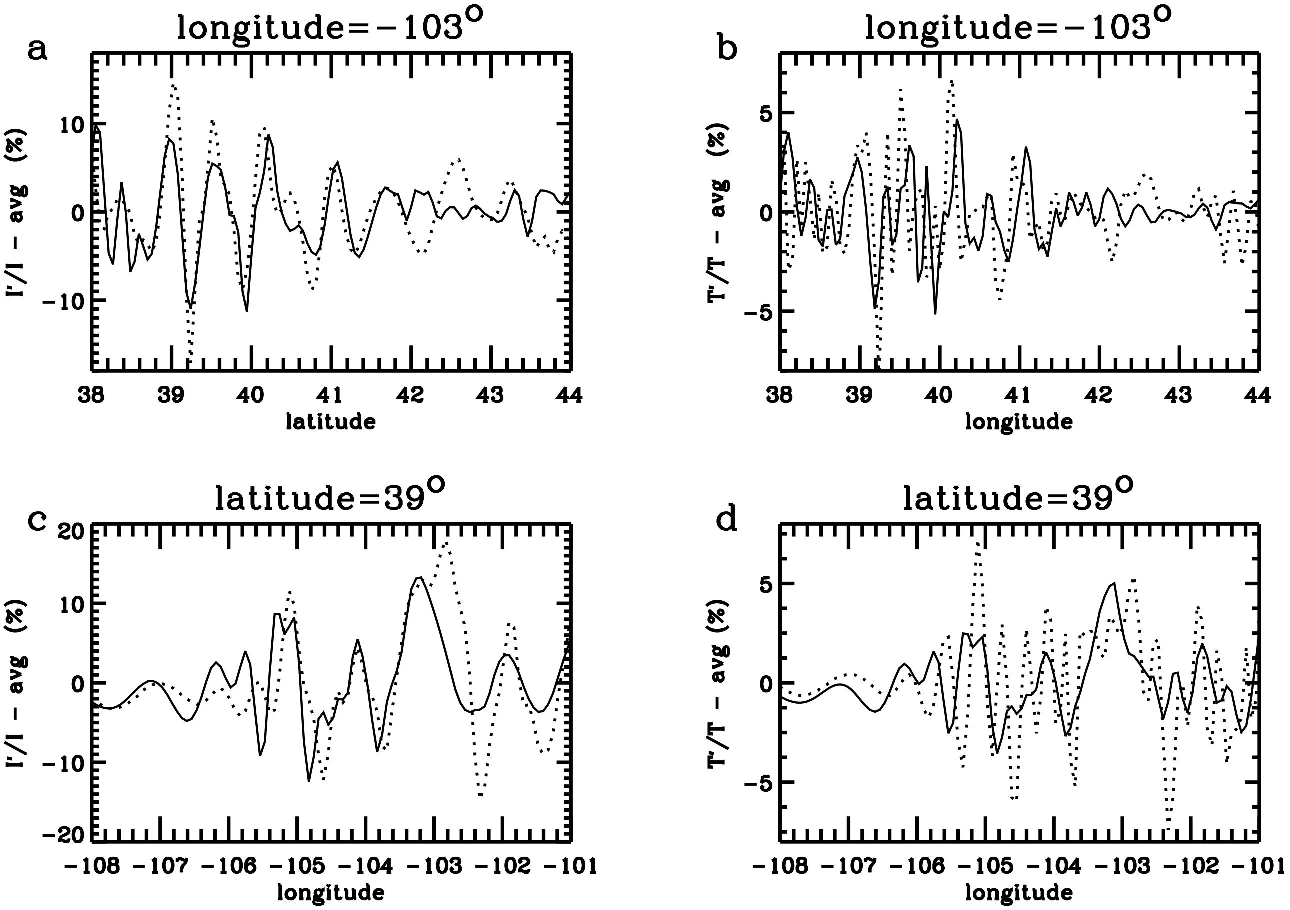

Figure 14. (a and c) $I'/\overline{I}$ and (b and d) $T'/\overline{T}$ at z = 86 km at 0300 UT from the ray trace results shown in Figure 12 using the background wind model (solid). Shown are the results at 103W (Figures 14a and 14b) and 39N (Figures 14c and 14d). The zero wind results (from Figure 13) are shown with dotted lines.

affected by the mean wind. At 0300 UT, GWs excited by a storm in eastern Colorado and storm 3 in South Dakota are dominant. However, GWs from storm 1 and from a storm in SW Colorado are also observed. Additionally, weak concentric GWs excited by storm 2 in Nebraska can be seen. This is in reasonable agreement with the OH image in Figure 2a, which only has good data north of 40N because of clouds. However, the model intensity perturbations from the storm at 38.5N in eastern Colorado are stronger than those from storm 1 (in NE Colorado), in contrast to the observations (see Figure 2a). From 0400 to 0430 UT, storm 1 creates somewhat stronger OH perturbations than storm 3, in agreement with the data.

[40] At later times, the GW patterns from the model wind are much more realistic than from the zero wind. A general feature is that the westward propagating waves often have larger amplitudes than the eastward GWs (e.g., Figures 12a, 12b, and 12d–12f), in good agreement with the observations. This is due to the eastward background winds. In addition, northwestward propagating GWs with short horizontal wavelengths generated by storm 1 are striking features in Figures 2e–2i (103–107W, 39–43N). These GWs are ubiquitous in Figures 12e–12i, although absent in Figures 13e–13i. Likewise, SWward propagating GWs from storm 3 with short horizontal wavelengths are dominant in Figures 2j–2l (102–106W, 38–41N). Although they cannot be seen in Figures 13j–13l, they are readily visible at 40–43N in Figures 12j–12l, although only north of 40N.

[41] There are also some disagreements between the model results and observations. For example, there are GWs excited by a storm in western Kansas (101.5W, 39.5N) which appear in the model results from 0630 to 0830 UT, but were not observed by the imager. Additionally, there are GWs from storms in southern Colorado and northern New Mexico which clearly appear in the model results, but are difficult to see in the airglow images (see the blue arrow in Figure 2l). However, clouds do obscure some of the GWs at that time in the southwest corner of the image (south of 39N). It is perhaps possible that there are larger meridional winds in the upper stratosphere and mesosphere south of 40N that are not accounted for in the TIME-GCM winds, and which filter the observed northward-propagating GWs (either through critical levels if the winds are large and northward, or through evanescence and reflection if the winds are large and southward).

[42] The intrinsic frequency of a zonally propagating GW at altitude z is

$$\omega_I(z) = \omega_I(z_{trop}) - k_h \Delta U \qquad (9)$$

where *trop* is tropopause and ΔU = U(*z*) − U_{trop}. Around 70 km, the model (i.e., TIME-GCM) zonal wind was westward, with U = -10 m/s (see Figure 11). Using the tropopause wind from Figure 10, ΔU is -20 to -40 m/s. Thus for an eastward-propagating, high-frequency GW with large k_h (i.e., short horizontal wavelength), its intrinsic frequency can increase to equal N near z = 70 km, whereby it reflects downward. This explains the absence of the eastward propagating waves in Figure 12 at late times (when the short horizontal-wavelength, slowly moving GWs reach the OH layer). By the same mechanism, the SWward-propagating GWs are Doppler-shifted within the OH layer to larger frequencies and larger λ_z in an eastward wind. During the later half of the night, the zonal model wind is 20 m/s toward the east at 87 km (see Figure 11). Since CF increases when λ_z increases, these SWward-propagating GWs are easier to see in the model wind than in a zero wind. This is one of the reasons $I'/\overline{I}$ is large for these GWs. The other reason concerns the increase in $T'/\overline{T}$ from some of the GWs nearing reflection levels, as we will discuss in a moment.

[43] We now examine the simulation results in more detail at 0300 UT. Figure 14 show slices of the model (solid) and zero (dotted) background wind results of the intensity and temperature perturbations at 103W and 39N. For the zero and model wind cases, the intensity perturbations from the GWs excited by the strong cluster in northeastern Colorado (storm 1) have amplitudes (at 103W and 40–41N, or 104W and 39N) of 4–9% and 4–8%, respectively. These results compare very well with the observed amplitude of ~5–8% from Figures 5b and 5c. For the zero and model wind cases, the intensity perturbations from the GWs excited by storm 3 (103W and 43N) are 2–4% and 1–3%, respectively. These values are quite similar to the observed values of ~3–4% (see Figure 5d). For the zero and model wind cases, the temperature perturbations from the GWs from the strong cluster in storm 1 are 2–4% and 2–5%, respectively. This is comparable to the measurement-based temperature perturbations of 1.4–2.3%.

[44] We wish to better understand the striking presence of the short horizontal wavelength SWward GWs at late times in the model wind results (e.g., at 0800 UT, 105W and north of 40N). Figure 15 shows slices at 0800 UT using the model and zero background wind results at 105W and 42N. We also display the average GW parameters (such as wave period and wavelengths), where the parameter in each bin is weighted by the GW's momentum flux [*Vadas and Fritts*, 2009, equation (66)]. The top row of each figure shows the OH intensity and temperature perturbations at 105W. At latitudes >40N, $T'/\overline{T} \sim 0.2$–0.4% and $I'/\overline{I} \sim 0.1$–0.3% for GWs with large horizontal wavelengths of $\lambda_h \sim 80$–110 km in the zero wind case. Since CF ~ 1, these GWs therefore have estimated vertical wavelengths of $|\lambda_z| \sim 15$ km (from Figure 4), and therefore have intrinsic periods of 15–30 min using equation (3). At latitudes >40N, $T'/\overline{T} \sim 1$–2% and $I'/\overline{I} \sim 2$–6% for GWs with smaller horizontal wavelengths of $\lambda_h \sim 30$–40 km in the model wind case. Since CF ~ 2, these GWs therefore have $|\lambda_z| \sim 20$ km, and therefore have frequencies close to the buoyancy frequency.

[45] Figures 15c–15h show the simulation results at 42N. For the model wind results, $|\lambda_z|$ increases slowly east of 107W, since the vertical wave number, m, begins to approach zero. Referring to equation (3), this occurs when the intrinsic phase speed, $c_h - U_h$, increases significantly. We are interested in the small-scale GWs at 105–106W. While the zero wind results only show the presence of large-scale GWs with $\lambda_h \sim 80$ km, $\tau \sim 30$ min, $c_h \sim 40$–50 m/s, and small temperature perturbations of $T'/\overline{T} \sim 0.2$–0.3%, the model wind results show the presence of GWs with $\lambda_h \sim 35$–40 km, $\tau \sim 12$–15 min, intrinsic phase speeds of $c_{Ih} \sim 40$–50 m/s, and much larger temperature perturbations of $T'/\overline{T} \sim 1$–1.5%. Since the smaller-scale GWs with $\lambda_h \sim 35$–40 km must be present in the zero wind result (since no wind filtering occurs), they must have had temperature perturbations smaller than 0.05% in order to not be easily visible in Figure 15d (dotted line). Note that the averaged, non-dimensional GW amplitudes are less than 0.15 in Figure 15h, which implies that these particular GWs did not saturate. (However, note that other GWs at this time, but at lower latitudes, did saturate.) Note that there is no clear evidence of wave breaking (turbulence or ripples [e.g., *Yue et al.*, 2010]) in the OH airglow observations on 8 September 2005 (Figure 2).

[46] The temperature perturbation of a GW with $|\lambda_z| < 4\pi$H [e.g., *Fritts and Alexander*, 2003; V09] is $T'/\overline{T} = -i[(g-1)/(Hg\omega_I)]w'$, where w' and u_h' are the GW vertical and horizontal velocity perturbations. Using equation (3) and the continuity equation $k_h u_h' = -mw'$, the temperature perturbation for a GW with $m^2 \gg k_h^2$ is

$$T'/\overline{T} \sim i[(g-1)/(HgN)](u_h'w')/w'. \qquad (10)$$

For a non-dissipating GW, the average of $\rho u_h'w'$ over a wave period is constant with altitude [*Andrews et al.*, 1987], where $u_h'w'$ is the momentum flux (per unit mass) and ρ is the background density. Since $u_h'w'$ (z_{trop}) is fixed, $u_h'w'$ at z = 86 km is the same whether a convectively excited GW propagates through the model or zero wind. Then, $T'/\overline{T}$ is proportional to $1/w'$ from equation (10). A GW which propagates against the wind and is near reflection has a smaller w' and larger $|\lambda_z|$, and therefore a larger $T'/\overline{T}$ than the equivalent GWs in a zero wind. This is seen in Figures 15d and 15g. This is the reason why the small-scale GWs at 105–106W and 42N have much larger $T'/\overline{T}$ when propagating against the background wind than in a zero wind. (Note that because $|\lambda_z| \ll \lambda_h$ at 105–106W from Figure 15g, the approximation, $m^2 \gg k_h^2$, is well-satisfied.) This effect, combined with the CF effect discussed above, is the reason the SWward short-wavelength GWs appear in the model (but not zero) wind results at late times.

[47] We now determine the source of the small-scale GWs at ~106W and ~42N and 0800 UT in Figure 12k. From Figure 15 for the model background wind, we estimate average wave parameters of $\lambda_h = 40$ km, $|\lambda_z| = 20$ km, $\tau = 25$ min and $\tau_I = 15$ min. Note that since the wind at (105W, 41N) and z = 86 km was mostly eastward in the model (i.e., U = 23 m/s, V = -6 m/s), the propagation of westward GWs is favored. This causes $\tau_I < \tau$. Because concentric GWs propagating NWward and SWward are constructively/destructively interfering at this location, these average quantities should be viewed as approximate values. Using equations (3) and (4), and assuming that the average intrinsic period of the GWs from the tropopause to the OH airglow layer is 20 min, we estimate a vertical group velocity of ~4.2 m/s. This yields a propagation time from the tropopause

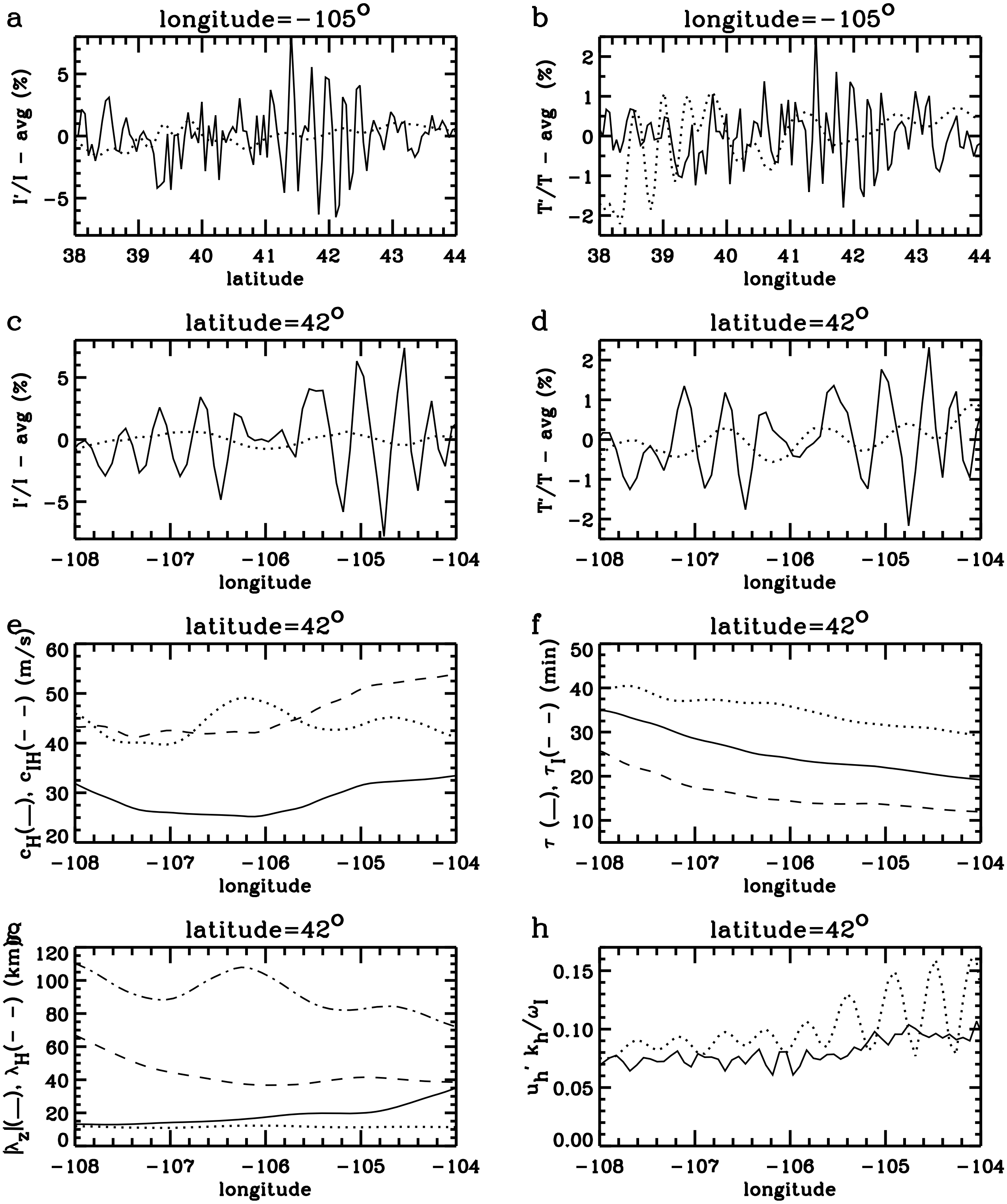

Figure 15. Results at 0800 UT and z = 86 km, using the ray trace results from Figures 12–13 at (a and b) 105W, and (c–g) 42N. Unless noted otherwise, the model wind results are shown with solid lines, and the zero wind results are shown with dotted lines. Shown are intensity perturbations, $I'/\overline{I}$ (Figure 15a), temperature perturbations, $T'/\overline{T}$ (Figure 15b), $I'/\overline{I}$ (Figure 15c), $T'/\overline{T}$ (Figure 15d), average observed (c_h, solid) and intrinsic (c_{Ih}, dashed) phase speeds (Figure 15e), average observed (τ, solid) and intrinsic (τ_I, dashed) wave periods (Figure 15f), average vertical wavelength $|\lambda_z|$ (solid and dotted lines for model and zero winds, respectively) and horizontal wavelength (λ_h, dashed and dashed-dotted lines for model and zero winds, respectively) (Figure 15g), and average non-dimensional amplitude, $u_h' k_h/\omega_I$ (Figure 15h).

to z = 86 km of 4.8 h, and an estimated source time of ~0310 UT. Using the model wind, we reverse ray-trace the SWward-propagating GWs from 0800 UT, 106W, and 42N, assuming wave parameters of τ = 24–27 min and an angle of azimuth of $\theta = -125°$ from north. These GWs reach the tropopause 4.4–5 h earlier at ~102.7–103.0W and ~43.7–43.9N. The strongest convective objects which correspond to these times and locations are 1) a cluster containing plumes with diameters of 20 km and updraft velocities of 75 m/s at 101W, 44N, and 0325 UT, and 2) a single plume with a 15 km diameter and an updraft velocity of 63 m/s at 102.5W, 44.0N, and 0305 UT.

[48] To further investigate this, we forward ray-trace a GW with λ_h = 40 km, τ = 27 min, and $\theta = -115°$ from this cluster. If this GW propagates through zero wind, it reaches z = 86 km at 0730 UT, 104.8W, and 42.6N, with $|\lambda_z|$ = 8 km. If this GW propagates through the model wind, then it reaches z = 86 km at 0808 UT, 105.4W and 42.5N, with $|\lambda_z|$ = 16 km. The CFs for $|\lambda_z|$ = 8 and 16 km are 0.035 and 1.4, respectively. This Doppler effect causes the OH intensity perturbations created by these small-scale, slowly moving GWs to be ~40 times larger for the model wind as compared to the zero wind. This, along with the increase in $T'/\overline{T}$ as GWs near reflection and w' decreases, is why the model wind simulates the slowly propagating, smaller-$|\lambda_z|$ GWs at late times more realistically than the zero wind.

[49] We now determine the dominant convective source of the small-scale GWs at ~106W, 42N and 0800 UT. We separately ray-trace the GWs excited by the following convective objects through the model background wind: (1) the cluster containing plumes with average diameters of 20 km and updraft velocities of 75 m/s at 101W, 44N, and 0325 UT, and (2) the single plume with a 15 km diameter and an updraft velocity of 63 m/s at 102.5W, 44.0N, and 0305 UT. For each, we apply Lindzen's saturation scheme for all 236 plumes/clusters/complexes from run 1, as described previously. We show the result at 0800 UT in Figure 16 for this cluster (upper 2 rows) and single plume (lower 2 rows). First, there are no GWs within 300 km of the centers of these convective objects at this late time. This is because GWs with small radii have large frequencies (see equation (2)), and therefore relatively large vertical group velocities (see equation (4)); these fast GWs would have reached the OH airglow layer prior to 0800 UT. Second, the regions where the GWs near reflection (i.e., where the average $|\lambda_z|$ increases significantly) are different, because of the different GW amplitudes. Third, there are GWs at ~106W and ~42N from both the cluster and the plume. Those from the cluster and plume have horizontal wavelengths of $\lambda_h \sim 60$ km and $\lambda_h \sim 35$ km, respectively. Those from the single plume agree better with Figure 15g (for the model wind). Most importantly, the OH intensity perturbations created by the GWs from the single plume, being ~1.5% at this location, are nearly ~30 times larger than those created by the GWs from the cluster. This value agrees well with Figure 15c (for the model wind). Additionally, the GWs from the single plume are propagating SWward, rather than nearly westward as for the GWs from the cluster. Therefore, we conclude that small-scale GWs in Figure 12k at this location at 0800 UT were likely excited by the strong single plume at 102.5W and 44N in South Dakota ~5 h earlier.

5. Conclusion

[50] This paper presents the finest observations, to date, of concentric GWs in the MLT. The observations were made with an all-sky OH imager near Fort Collins, Colorado, on the night of 08 September 2005, and lasted for nearly 6 h. By comparing these observations with GOES IR satellite images and NEXRAD radar maps, we find that the epicenters of the concentric rings overlay well with the strong convective plumes; therefore, these GWs were generated by multiple severe thunderstorms hundreds of kilometers apart on the Great Plain. The strongest thunderstorms were located in northeastern Colorado, western Nebraska, and southwestern South Dakota. We also find that the GWs closely followed the thunderstorms; in particular, GWs were observed tens of minutes after the onset of strong updrafts. Hailstorms were reported near the epicenters of the GWs.

[51] Unlike the simpler 11 May 2004 event described in Y09, because deep convection was long-lasting and occurred in many locations, the GWs from different updrafts constructively or destructively interfered with each other. The observed GWs have $\lambda_h \sim$ 15–35 km, $\tau \sim$ 7–12 min, $c_h \sim$ 20–80 m/s at radii of R ~ 80–300 km from their sources. We find that the time evolution of the observed wave parameters obeys the GW dispersion relation; GWs at the same radii with shorter horizontal wavelengths have smaller vertical group velocities, therefore reach the airglow layer later than waves with longer wavelengths. Using the background horizontal wind measurement by a local MF radar, we calculate their vertical wavelengths, propagation times, and temperature perturbations. We estimate temperature perturbations of ~1–3% for the GWs at z = 86 km from strong convective clusters.

[52] We also modeled the excitation and propagation of GWs excited by deep convective plumes during the 8-h period from 0100 to 0900 UT. The plume parameters, locations, and times of these convective objects were identified from GOES satellite images, and the updraft velocities were calculated from CAPE maps. We used a convective plume model to generate GWs from these convective objects, then ray-traced them from the tropopause to the OH airglow layer through a background model (based on radiosonde/TIME-GCM data) and zero wind. We then reconstructed the GW temperature perturbations, and computed the approximate OH intensity perturbations using an analytic formula for the cancellation factor. We find that the results agree well with the observations when using the model background winds, especially at late times (after 0530 UT) when SWward-propagating GWs with small horizontal wavelengths and high frequencies reached the OH airglow. These GWs were found to propagate against the wind. The zero wind results showed no evidence of these GWs. The appearance of these small-scale GWs in the model wind case was found to be due to 1) the increase of the temperature perturbations when w' decreases because the GWs are nearing reflection, and 2) to the enhanced vertical wavelengths from this Doppler-shifting, which causes an enhanced CF and larger intensity perturbations. This effect is important when GWs propagate against the background wind, thereby increasing $|\lambda_z|$ to be >10 km.

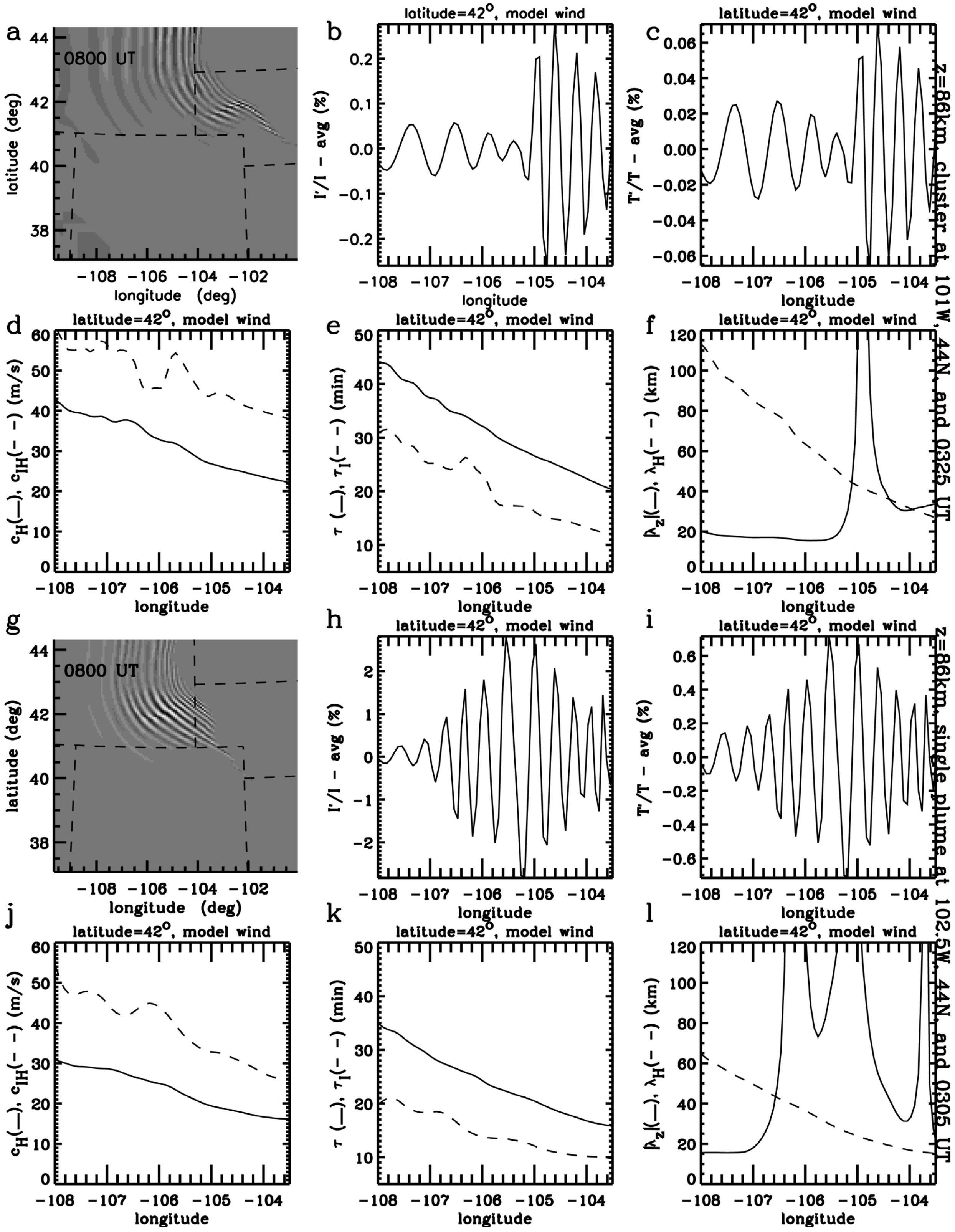

Figure 16. (a–f) Results at 0800 UT and z = 86 km for ray tracing the excited GWs from the cluster at 101W, 44 N, and 0325 UT through the background wind model. $I'/\bar{I}$ (Figure 16a) and $I'/\bar{I}$ at 42N (Figure 16b), $T'/\bar{T}$ at 42N (Figure 16c), average observed (c_h, solid) and intrinsic (c_{Ih}, dashed) phase speeds at 42N (Figure 16d), average observed (τ, solid) and intrinsic (τ_I, dashed) wave periods at 42N (Figure 16e), average vertical wavelength ($|\lambda_z|$, solid line) and horizontal wavelength (λ_h, dashed line) at 42N (Figure 15f). (g–l) Same as Figures 16a–16f but for the single plume at 102.5W, 44.0N, and 0305 UT.

[53] We then reverse ray traced these late-time, SWward propagating GWs from 105W and 42N, and found they originated 5 h earlier from a deep convective plume in S. Dakota. These results therefore confirm the possibility that some of the small-scale GWs observed in the OH layer can propagate directly from the tropopause. (Other possibilities for these small-scale GWs is that they are created from nearby GW breaking, or are ducted within the mesopause region from a more remote location.)

[54] The Great Plain is an ideal location to observe convectively generated GWs [Y09; *Hoffmann and Alexander*, 2010]. Concentric GWs are particularly useful for GW studies, if available, because there is less influence from background winds. If the background winds are strong, then convectively generated GWs will appear instead as planar waves in the OH images. In the later case, planar waves can also be useful if the winds between the tropopause and mesopause are known reasonably well. Coordinated ground-based airglow and space-born observations of concentric GWs can yield further information on the amplitudes and parameters of GWs excited by deep convection, and their effects at higher altitudes. For example, at 0800 UT on 03 June 2008, the same groups of concentric GWs were concurrently observed by the YR airglow imager (see Figure 2 of Y09) and the Atmospheric Infrared Sounder (AIRS) [*Hoffmann and Alexander*, 2010; L. Hoffmann, personal communication, 2011]. This is left for future study.

[55] To accurately model the convective GWs propagating into the MLT, hourly background wind information is desired. Most radiosondes launch twice a day, and the empirical or first principle models such as the TIME-GCM are not able to accurately predict the day-to-day and hour-to-hour wind variations. Yet the accuracy of the ray-trace results is limited by the accuracy of the background wind model. Concurrent wind measurements extending from the ground to the MLT, such as Mie/Rayleigh/Doppler/resonance lidars [*Baumgarten*, 2010], will help dramatically improve the accuracy of the GW ray-trace model results.

[56] **Acknowledgments.** The authors are in great debt to Denise Thorsen for providing the Platteville MF radar data. J.Y. would like to thank Ben Foster and Ray Roble for helping to perform the TIME-GCM simulations. We are grateful to Walter Lyons for maintaining the imager observation at YRFS. We thank Pete Stamus for generating the plume/cluster/complex parameters from the GOES IR satellite images and CAPE maps. J.Y. acknowledges Ingrid Cnossen and Joe She for helpful comments on the early draft. J.Y. was supported by the National Center for Atmospheric Research, which is sponsored by the National Science Foundation. S.L.V. was supported by NSF grant ATM-0836195, and NASA contracts NNH08CE12C and NNH10CC98C. The observation of the OH imager in Colorado and TN was supported by JSPS Grant-in-Aid for Scientific Research (B) (14403008 and 20403011).

References

Alexander, M. J., J. R. Holton, and D. R. Durran (1995), The gravity wave response above deep convection in a squall line simulation, *J. Atmos. Sci.*, *52*(12), 2212–2226, doi:10.1175/1520-0469(1995)052<2212:TGWRAD>2.0.CO;2.

Alexander, M. J., P. T. May, and J. H. Beres (2004), Gravity waves generated by convection in Darwin area during the Darwin Area Wave Experiment, *J. Geophys. Res.*, *109*, D20S04, doi:10.1029/2004JD004729.

Andrews, D. G., J. R. Holton, and C. B. Leovy (1987), *Middle Atmosphere Dynamics*, Academic, San Diego, Calif.

Baumgarten, G. (2010), Doppler Rayleigh/Mie/Raman lidar for wind and temperature measurements in the middle atmosphere up to 80 km, *Atmos. Meas. Tech.*, *3*(6), 1509–1518, doi:10.5194/amt-3-1509-2010.

Beres, J. H. (2004), Gravity wave generation by a three-dimensional thermal forcing, *J. Atmos. Sci.*, *61*, 1805–1815, doi:10.1175/1520-0469(2004)061<1805:GWGBAT>2.0.CO;2.

Choi, H.-J., H.-Y. Chun, and I.-S. Song (2007), Characteristics and momentum flux spectrum of convectively forced internal gravity waves in ensemble numerical simulations, *J. Atmos. Sci.*, *64*(10), 3723–3734, doi:10.1175/JAS4037.1.

Chun, H.-Y., H.-J. Choi, and I.-S. Song (2008), Effects of nonlinearity on convectively forced internal gravity waves: Application to a gravity wave drag parameterization, *J. Atmos. Sci.*, *65*(2), 557–575, doi:10.1175/2007JAS2255.1.

Dewan, E. M., R. H. Picard, R. R. O'Neil, H. A. Gardiner, J. Gibson, J. D. Mill, E. Richards, M. Kendra, and W. O. Gallery (1998), MSX satellite observations of thunderstorm-generated gravity waves in mid-wave infrared images of the upper stratosphere, *Geophys. Res. Lett.*, *25*(7), 939–942, doi:10.1029/98GL00640.

Eckermann, S., and C. Marks (1996), An idealized ray model of gravity wave tidal interactions, *J. Geophys. Res.*, *101*(D16), 21,195–21,212, doi:10.1029/96JD01660.

Fritts, D. C., and M. J. Alexander (2003), Gravity wave dynamics and effects in the middle atmosphere, *Rev. Geophys.*, *41*(1), 1003, doi:10.1029/2001RG000106.

Garcia, F. J., M. J. Taylor, and M. C. Kelley (1997), Two-dimensional spectral analysis of mesospheric airglow image data, *Appl. Opt.*, *36*(29), 7374–7385, doi:10.1364/AO.36.007374.

Garcia, R. R., and S. Solomon (1985), The effect of breaking gravity waves on the dynamics and chemical composition of the mesosphere and lower thermosphere, *J. Geophys. Res.*, *90*(D2), 3850–3868, doi:10.1029/JD090iD02p03850.

Grimsdell, A. W., M. J. Alexander, P. T. May, and L. Hoffmann (2010), Model study of waves generated by convection with direct validation via satellite, *J. Atmos. Sci.*, *67*, 1617–1631, doi:10.1175/2009JAS3197.1.

Hecht, J. H., T. J. Kane, R. L. Walterscheid, C. S. Gardner, and C. A. Teplky (1993), Simultaneous nightglow and Na lidar observations at Arecibo during the AIDA-89 campaign, *J. Atmos. Sol. Terr. Phys.*, *55*, 409–423, doi:10.1016/0021-9169(93)90077-C.

Hickey, M. (1988a), Effects of eddy viscosity and thermal conduction and Coriolis force in the dynamics of gravity wave driven fluctuations in the OH nightglow, *J. Geophys. Res.*, *93*(A5), 4077–4088, doi:10.1029/JA093iA05p04077.

Hickey, M. (1988b), Wavelength dependence of eddy dissipation and Coriolis force in the dynamics of gravity wave driven fluctuations in the OH nightglow, *J. Geophys. Res.*, *93*(A5), 4089–4101, doi:10.1029/JA093iA05p04089.

Hickey, M. P., and J. S. Brown (2002), A simulation study of space-based observations of waves in the airglow using observed ALOHA-93 wave parameters, *J. Geophys. Res.*, *107*(A12), 1431, doi:10.1029/2001JA009225.

Hickey, M. P., and Y. Yu (2005), A full-wave investigation of the use of a "cancellation factor" in gravity wave-OH airglow interaction studies, *J. Geophys. Res.*, *110*, A01301, doi:10.1029/2003JA010372.

Hines, C. O. (1967), On the nature of travelling ionospheric disturbances launched by low-altitude nuclear explosions, *J. Geophys. Res.*, *72*, 1877–1882, doi:10.1029/JZ072i007p01877.

Hines, C. O., and D. W. Tarasick (1987), On the detection and utilization of gravity waves in airglow studies, *Planet. Space Sci.*, *35*, 851–866, doi:10.1016/0032-0633(87)90063-8.

Hoffmann, L., and M. J. Alexander (2010), Occurrence frequency of convective gravity waves during the North American thunderstorm season, *J. Geophys. Res.*, *115*, D20111, doi:10.1029/2010JD014401.

Holton, J. R. (1982), The role of gravity wave induced drag and diffusion in the momentum budget of the mesosphere, *J. Atmos. Sci.*, *39*, 791–799, doi:10.1175/1520-0469(1982)039<0791:TROGWI>2.0.CO;2.

Holton, J. R., and M. J. Alexander (1999), Gravity waves in the mesosphere generated by tropospheric convection, *Tellus, Ser. A-B*, *51*, 45–58.

Horinouchi, T., T. Nakamura, and J.-I. Kosaka (2002), Convectively generated mesoscale gravity waves simulated throughout the middle atmosphere, *Geophys. Res. Lett.*, *29*(21), 2007, doi:10.1029/2002GL016069.

Krassovsky, V. I. (1972), Infrasonic variations of OH emissions in the upper atmosphere, *Ann. Geophys.*, *28*, 739–746.

Lane, T. P., M. J. Reeder, and T. L. Clark (2001), Numerical modeling of gravity waves generated by deep tropical convection, *J. Atmos. Sci.*, *58*, 1249–1274.

Lane, T. P., and R. D. Sharman (2006), Gravity wave breaking, secondary wave generation, and mixing above deep convection in a three dimensional cloud model, *Geophys. Res. Lett.*, *33*, L23813, doi:10.1029/2006GL027988.

Lane, T. P., R. D. Sharman, T. L. Clark, and H.-M. Hsu (2003), An investigation of turbulence generation mechanisms above deep convection, *J. Atmos. Sci.*, *60*, 1297–1321, doi:10.1175/1520-0469(2003)60<1297:AIOTGM>2.0.CO;2.

Lighthill, J. (1978), *Waves in Fluids*, Cambridge Univ. Press, Cambridge, U. K.

Lin, Y.-L., and H.-Y. Chun (1991), Effects of diabatic cooling in a shear flow with a critical level, *J. Atmos. Sci.*, *48*(23), 2476–2491, doi:10.1175/1520-0469(1991)048<2476:EODCIA>2.0.CO;2.

Lindzen, R. S. (1981), Turbulence and stress owing to gravity wave and tidal breakdown, *J. Geophys. Res.*, *86*(C10), 9707–9714, doi:10.1029/JC086iC10p09707.

Liu, A. Z., and G. R. Swenson (2003), A modeling study of O_2 and OH airglow perturbations induced by atmospheric gravity waves, *J. Geophys. Res.*, *108*(D4), 4151, doi:10.1029/2002JD002474.

Manson, A. H., C. E. Meek, S. K. Avery, and D. Thorsen (2003), Ionospheric and dynamical characteristics of the mesosphere-lower thermosphere region over Platteville (40°N, 105°W) and comparisons with the region over Saskatoon (52°N, 107°W), *J. Geophys. Res.*, *108*(D13), 4398, doi:10.1029/2002JD002835.

Nakamura, T., T. Fukushima, T. Tsuda, C. Y. She, B. P. Williams, D. Krueger, and W. Lyons (2005), Simultaneous observation of dual-site airglow imagers and a sodium temperature-wind lidar, and effect of atmospheric stability on the airglow structure, *Adv. Space Res.*, *35*, 1957–1963, doi:10.1016/j.asr.2005.05.102.

Pandya, R. E., and M. J. Alexander (1999), Linear stratospheric gravity waves above convective thermal forcing, *J. Atmos. Sci.*, *56*(14), 2434–2446, doi:10.1175/1520-0469(1999)056<2434:LSGWAC>2.0.CO;2.

Piani, C., D. Durran, M. J. Alexander, and J. R. Holton (2000), A numerical study of three-dimensional gravity waves triggered by deep tropical convection and their role in the dynamics of the QBO, *J. Atmos. Sci.*, *57*(22), 3689–3702, doi:10.1175/1520-0469(2000)057<3689:ANSOTD>2.0.CO;2.

Pierce, A. D., and S. C. Coroniti (1966), A mechanism for the generation of acoustic-gravity waves during thunderstorm formation, *Nature*, *210*, 1209–1210, doi:10.1038/2101209a0.

Pitts, D. E., et al. (1995), Earth observations during space shuttle mission STS-55: *Columbia's* mission to planet Earth (April 26 - May 6, 1993), *Geocarto Int.*, *10*(1), 67–79, doi:10.1080/10106049509354481.

Renick, J. H., and J. B. Maxwell (1977), Forecasting hailfall in Alberta, *Meteorol. Monogr.*, *38*, 145–151.

Roble, R. G., and E. C. Ridley (1994), A thermosphere ionosphere mesosphere electrodynamics general circulation model (time-GCM): Equinox solar cycle minimum simulations (30–500 km), *Geophys. Res. Lett.*, *21*(6), 417–420, doi:10.1029/93GL03391.

Schubert, G., and R. Walterscheid (1988), Wave-driven fluctuations in OH nightglow from an extended source region, *J. Geophys. Res.*, *93*(A9), 9903–9915, doi:10.1029/JA093iA09p09903.

Sentman, D. D., E. M. Wescott, R. H. Picard, J. R. Winick, H. C. Stenbaek Nielsen, E. M. Dewan, D. R. Moudry, F. T. Sao Sabbas, M. J. Heavner, and J. Morrill (2003), Simultaneous observations of mesospheric gravity waves and sprites generated by a midwestern thunderstorm, *J. Atmos. Terr. Phys.*, *65*, 537–550, doi:10.1016/S1364-6826(02)00328-0.

Smith, S. A., D. C. Fritts, and T. E. Vanzandt (1987), Evidence for a saturated spectrum of atmospheric gravity waves, *J. Atmos. Sci.*, *44*, 1404–1410, doi:10.1175/1520-0469(1987)044<1404:EFASSO>2.0.CO;2.

Smith, S., M. Mendillo, J. Baumgardner, and R. Clark (2000), Mesospheric gravity wave imaging at a subauroral site: First results from Millstone Hill, *J. Geophys. Res.*, *105*(A12), 27,119–27,130, doi:10.1029/1999JA000343.

Song, I.-S., H.-Y. Chun, and P. P. Lane (2003), Generation mechanisms of convectively forced internal gravity waves and their propagation to the stratosphere, *J. Atmos. Sci.*, *60*, 1960–1980, doi:10.1175/1520-0469(2003)060<1960:GMOCFI>2.0.CO;2.

Stull, R. B. (1976), Internal gravity waves generated by penetrative convection, *J. Atmos. Sci.*, *33*(7), 1279–1286, doi:10.1175/1520-0469(1976)033<1279:IGWGBP>2.0.CO;2.

Suzuki, S., K. Shiokawa, Y. Otsuka, T. Ogawa, K. Nakamura, and T. Nakamura (2007), A concentric gravity wave structure in the mesospheric airglow images, *J. Geophys. Res.*, *112*, D02102, doi:10.1029/2005JD006558.

Swenson, G. R., and C. S. Gardner (1998), Analytical models for the responses of the mesospheric OH* and Na layers to atmospheric gravity waves, *J. Geophys. Res.*, *103*, 6271–6294, doi:10.1029/97JD02985.

Swenson, G. R., M. J. Taylor, P. J. Espy, C. Gardner, and X. Tac (1995), ALOHA-93 measurements of intrinsic AGW characteristics using airborne airglow imager and groundbased Na wind/temperature lidar, *Geophys. Res. Lett.*, *22*(20), 2841–2844, doi:10.1029/95GL02579.

Taylor, M. J., and M. A. Hapgood (1988), Identification of a thunderstorm as a source of short period gravity waves in the upper atmospheric nightglow emissions, *Planet. Space Sci.*, *36*, 975–985, doi:10.1016/0032-0633(88)90035-9.

Taylor, M. J., M. B. Bishop, and V. Taylor (1995), All-sky measurements of short period waves imaged in the OI (557.7nm), Na(589.2nm) and near infrared OH and O_2 (0,1) nightglow emissions during the ALOHA-93 campaign, *Geophys. Res. Lett.*, *22*, 2833–2836, doi:10.1029/95GL02946.

Taylor, M. J., P.-D. Pautet, A. F. Medeiros, R. Buriti, J. Fechine, D. C. Fritts, S. L. Vadas, H. Takahashi, and F. T. São Sabbas (2009), Characteristics of mesospheric gravity waves near the magnetic equator, Brazil, during the SpreadFEx campaign, *Ann. Geophys.*, *27*, 461–472, doi:10.5194/angeo-27-461-2009.

Vadas, S. L., and G. Crowley (2010), Sources of the traveling ionospheric disturbances observed by the ionospheric TIDDBIT sounder near Wallops Island on 30 October 2007, *J. Geophys. Res.*, *115*, A07324, doi:10.1029/2009JA015053.

Vadas, S. L., and D. C. Fritts (2004), Thermospheric response to gravity waves arising from mesoscale convective complexes, *J. Atmos. Sol. Terr. Phys.*, *66*, 781–804, doi:10.1016/j.jastp.2004.01.025.

Vadas, S. L., and D. C. Fritts (2009), Reconstruction of the gravity wave field from convective plumes via ray tracing, *Ann. Geophys.*, *27*, 147–177, doi:10.5194/angeo-27-147-2009.

Vadas, S. L., and H. Liu (2009), Generation of large-scale gravity waves and neutral winds in the thermosphere from the dissipation of convectively generated gravity waves, *J. Geophys. Res.*, *114*, A10310, doi:10.1029/2009JA014108.

Vadas, S. L., D. C. Fritts, and M. J. Alexander (2003), Mechanism for the generation of secondary waves in wave breaking regions, *J. Atmos. Sci.*, *60*, 194–214, doi:10.1175/1520-0469(2003)060<0194:MFTGOS>2.0.CO;2.

Vadas, S. L., J. Yue, C.-Y. She, P. Stamus, and A. Z. Liu (2009a), A model study of the effects of winds on concentric rings of gravity waves from a convective plume near Fort Collins on 11 May 2004, *J. Geophys. Res.*, *114*, D06103, doi:10.1029/2008JD010753.

Vadas, S. L., M. J. Taylor, P.-D. Pautet, P. A. Stamus, D. C. Fritts, H.-L. Liu, F. T. Sao Sabbas, V. T. Rampinelli, P. Batista, and H. Takahashi (2009b), Convection: The likely source of medium-scale gravity waves observed in the OH airglow layer near Brasilia, Brazil, during the SpreadFEx Campaign, *Ann. Geophys.*, *27*, 231–259, doi:10.5194/angeo-27-231-2009b.

Wallace, J. M., and P. V. Hobbs (2006), *Atmospheric Science: An Introductory Survey*, Elsevier, New York.

Walterscheid, R., G. Schubert, and J. Straus (1987), A dynamical-chemical model of wave-driven fluctuations in the OH nightglow, *J. Geophys. Res.*, *92*(A2), 1241–1254, doi:10.1029/JA092iA02p01241.

Walterscheid, R. L., G. Schubert, and D. G. Brinkman (2001), Small-scale gravity waves in the upper mesosphere and lower thermosphere generated by deep tropical convection, *J. Geophys. Res.*, *106*(D23), 31,825–31,832, doi:10.1029/2000JD000131.

Yue, J., S. L. Vadas, C.-Y. She, T. Nakamura, S. C. Reising, H.-L. Liu, P. Stamus, D. A. Krueger, W. Lyons, and T. Li (2009), Concentric gravity waves in the mesosphere generated by deep convective plumes in the lower atmosphere near Fort Collins, Colorado, *J. Geophys. Res.*, *114*, D06104, doi:10.1029/2008JD011244.

Yue, J., T. Nakamura, C.-Y. She, M. Weber, W. Lyons and T. Li (2010), Seasonal and local time variability of ripples from airglow imager observations in US and Japan, *Ann. Geophys.*, *28*, 1401–1408, doi:10.5194/angeo-28-1401-2010.

T. Nakamura, National Institute of Polar Research, 10-3 Midoricho, Tachikawa, Tokyo 190-8518, Japan.

S. Vadas, NorthWest Research Associates, Inc., 3380 S. Mitchell Ln., Boulder, CO 80301, USA. (vasha@cora.nwra.com)

J. Yue, High Altitude Observatory, National Center for Atmospheric Research, Boulder, CO 80307-3000, USA.